# Measurement of the Branching Fraction of B anti-B --> $K^0_S$ X Decay at the *BABAR* Experiment

Alexander Tumanov

Stanford Linear Accelerator Center
Stanford University
Stanford, CA 94309

SLAC-Report-618
March 2003

Prepared for the Department of Energy
under contract number DE-AC03-76SF00515

# Measurement of the Branching Fraction of $B\overline{B} \to K^0_S X$ Decay at the *BABAR* Experiment

Alexander Tumanov

January 2002


Princeton University

Department of Physics

Thesis submitted to Princeton University for the degree of Doctor of Philosophy. Advisor: Professor A. J. Stewart Smith.

**Abstract**

This thesis presents various studies of $K_S^0$ mesons carried out at the *BABAR* experiment. Studying multiplicities of $K_S^0$ in $B\overline{B}$ decays provides deeper knowledge of the detector performance and produces an important physical result. The branching fraction of $B\overline{B} \to K_S^0 X$ decay is measured using $286\,pb^{-1}$ of data collected during the first year of physics running. The result obtained is $BR(B\overline{B} \to XK_S^0 \to \pi^+\pi^-) = 0.216 \pm 0.003(stat.) \pm 0.015(syst.)$. Implications of this result to the presence of the new physics at TeV scale are discussed. The momentum spectrum of $K_S^0$ coming from $B\overline{B} \to XK_S^0 \to \pi^+\pi^-$ is also presented.

# Contents

# Acknowledgments

This would not have been possible without the help and participation of a few fantastic people whom I would like to thank here. First, I should mention the *BABAR* collaboration itself was a great place to be in. I thank many dedicated people for their work in making the collaboration environment interesting and fulfilling for me as a student. I would like to thank the collaboration spokesperson and my advisor Professor Stew Smith for making my experience at *BABAR* intellectually nourishing. I also thank Stew for devoting his time to help me with the thesis document.

I would like to acknowledge friendly and helpful members of the physics analysis groups I have had a chance to work in: Charmonium group and its convener Riccardo Faccini and Inclusive Hadronic Spectra group and its convener Blair Ratcliff. I would like to especially mention my greatest gratitude to Tobias Haas who dedicated his time and patience to help me with his advice and insight.

Thanks to the following friends and colleagues for their help and encouragement: Justin Albert, Valery Miftahov, Timur Shutenko, Erich Varnes.

And last, but not least, I would like to thank my parents and especially

my mom for their love and support. I will try to accomplish the goals that you have set for me.

# Chapter 1

# Introduction to Topics in B Physics.

## 1.1 Introduction

This thesis studies decays of the B meson where one of the decay products is a $K_S^0$ meson, which we call inclusive B decays to $K_S^0$. The branching fraction as well as other important characteristics such as the $K_S^0$ momentum spectrum are measured. Results obtained are analyzed with the perspective of new physics processes at TeV scale [1] that can manifest in certain B physics processes. The experimental data used in this paper were collected within the *BABAR* detector in an experiment dedicated mainly to studying CP symmetry violation phenomena in B physics. $K_S^0$ study was one of the top priorities of the *BABAR* experiment and the author was actively involved in reconstructing $K_S^0$ since the very first data started to come in. A firm

understanding of efficiencies for $K_S^0$ is critical to measuring CP violation in that most of the easily accessible channels for CP violation involve $K_S^0$; e.g. $B^0 \to J/\Psi K_S^0$, $B^0 \to \Psi(2S)K_S^0$, $B^0 \to J/\Psi K^* \to K_S^0\pi$. In the course of my work on $K_S^0$ reconstruction I became interested in the physics of the $K_S^0$ spectrum itself.

In 1964 physicists from Princeton University - J. H. Christenson, J. W. Cronin, V. L. Fitch, and R. Turlay observed one of the most interesting phenomena in particle physics, the violation of CP symmetry in the decay of neutral kaons [2]. For thirty-seven years neutral kaons were the only system in which CP violation has been seen. However, even in advance of the discovery of the $\Upsilon$ in 1977, it was suspected that neutral B mesons could provide another system where CP asymmetries could be seen [3], [4].

The abbreviation CP stands for simultaneous charge conjugation C and parity reversal P operations. Charge conjugation interchanges particles with anti-particles. Parity, P, reverses space coordinates $(t, \overline{\mathbf{x}}) \to (t, -\overline{\mathbf{x}})$. The operation of time reversal, T, reverses the sign of time $(t, \overline{\mathbf{x}}) \to (-t, \overline{\mathbf{x}})$. The combination CPT is an exact symmetry in any local Lorentz invariant Lagrangian field theory [5]. However, separately Parity, Time and CP symmetry violations are possible and have been observed.

The origins of CP violation are still poorly understood. The Standard Model accommodates CP violation in the theory of weak interactions. In particular, B meson decays are predicted to exhibit clean CP asymmetries enabling us to make stringent tests of the Standard Model. Establishing CP violation in the B-meson system is of fundamental importance: it was

first noted by A. D. Sakharov that the observed dominance of the matter over the antimatter requires the CP symmetry to be violated in fundamental processes in the early universe[6]. And as it is speculated recently [7], [8], in order to see current levels of the baryon asymmetry the extent of the CP violation in the early universe should have been much larger than is predicted by the Standard Model. In addition, baryon number violation and thermal non-equilibrium are also required according to A. D. Sakharov. The topic of baryogenesis is very exciting and widely debated in the physics community [9], [10]. However, with the exception of our own existence, no experimental evidence supporting baryogenesis theories has been seen yet. Studying B mesons can shed light on this and other interesting puzzles and that is why today many major laboratories and institutions are engaged in B physics projects. Among them are such as CERN, DESY, FNAL, KEK, SLAC etc. Princeton University takes part in the *BABAR*(SLAC) and the Belle(KEK) projects. In July 2001 *BABAR* and Belle announced observation of the CP violation in neutral B meson system [12], [13]. Further in this chapter we will discuss the CP violation phenomena in detail.

## 1.2 CP Violation in the Standard Model

In the Standard Model the part of the electroweak Hamiltonian which describes $W$ boson coupling to quarks has the form:

$$H_W = \frac{g}{\sqrt{2}}\, W^{-\mu} \sum_{\substack{U=u,c,t \\ D=d,s,b}} V_{UD} \overline{U}_L \gamma_\mu D_L + \frac{g}{\sqrt{2}}\, W^{+\mu} \sum_{U,D} V^*_{UD} \overline{D}_L \gamma_\mu U_L \qquad (1.2.1)$$

Here $V_{UD}$ are the coefficients of a unitary $3\times3$ matrix called the Cabibbo-Kobayashi-Maskawa (CKM) matrix:

$$V_{CKM} = \begin{pmatrix} V_{ud} & V_{us} & V_{ub} \\ V_{cd} & V_{cs} & V_{cb} \\ V_{td} & V_{ts} & V_{tb} \end{pmatrix}$$

The off-diagonal elements of this matrix relate to the transitions between quarks of one family to another and therefore the matrix is also called the quark mixing matrix. It is interesting to note that initially the quark mixing matrix was assumed to be a $2 \times 2$ rotational matrix:

$$V_{Cabibbo} = \begin{pmatrix} V_{ud} & V_{us} \\ V_{cd} & V_{cs} \end{pmatrix} = \begin{pmatrix} 1-\lambda^2/2 & \lambda \\ -\lambda & 1-\lambda^2/2 \end{pmatrix}$$

The rotation angle, or Cabibbo angle, $\lambda$ was the only real parameter of this matrix and among four quarks predicted by this matrix - u, d, s, c - the charm quark, $c$, was still to be seen in an experiment. To accommodate CP violation in the weak interactions theory Kobayashi and Maskawa suggested the third generation of quarks and expanded the $2 \times 2$ Cabibbo matrix to the $3 \times 3$ Cabibbo-Kobayashi-Maskawa matrix [3].

Under CP transformation $H_W$ becomes[1]:

$$(CP)H_W(CP)^{-1} = (H_W)_{CP} =$$

[1]For more details see [14].

$$= \frac{g}{\sqrt{2}}\, W^{+\mu} \sum_{U,D} V_{UD} \overline{D}_L \gamma_\mu U_L + \frac{g}{\sqrt{2}}\, W^{-\mu} \sum_{U,D} V^*_{UD} \overline{U}_L \gamma_\mu D_L \qquad (1.2.2)$$

We see that if $V_{UD} = V^*_{UD}$ for any U, D then $(H_W)_{CP} = H_W$ and CP symmetry is not violated... The CKM matrix elements most generally are complex therefore there are 18 real parameters. However the unitarity of $V_{CKM}$ imposes the following conditions:

$$|V_{ud}|^2 + |V_{cd}|^2 + |V_{td}|^2 = 1$$

$$|V_{us}|^2 + |V_{cs}|^2 + |V_{ts}|^2 = 1$$

$$|V_{ub}|^2 + |V_{cb}|^2 + |V_{tb}|^2 = 1$$

$$V_{ud}V^*_{us} + V_{cd}V^*_{cs} + V_{td}V^*_{ts} = 0$$

$$V_{ud}V^*_{ub} + V_{cd}V^*_{cb} + V_{td}V^*_{tb} = 0$$

$$V_{us}V^*_{ub} + V_{cs}V^*_{cb} + V_{ts}V^*_{tb} = 0.$$

This reduces the number of independent real parameters to 9. Also, since the absolute phases of the quarks are not important, the phases of 5 elements of $V_{CKM}$ (one row and one column) could be canceled. Thus, we are left with only four independent coefficients: $\lambda, A,\ \rho$, and $\eta$. The CKM matrix can then be written in a form suggested by Wolfenstein[2]:

[2]This form is an approximation of the Unitarity matrix to $O(\lambda^3)$

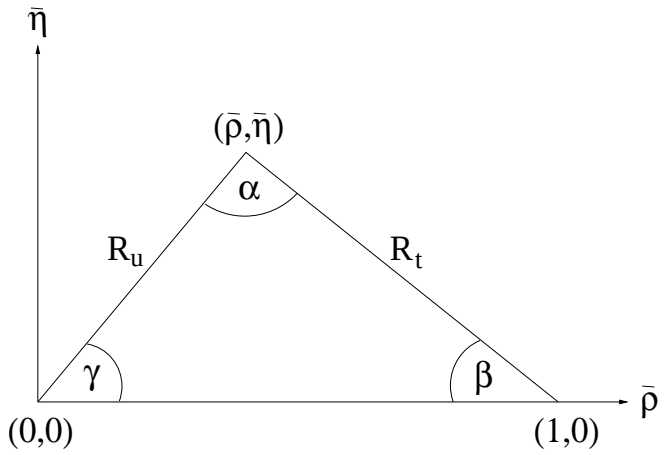


Figure 1.1: *Unitarity Triangle schematically shown in the* $(\eta, \rho)$ *plane.*

$$\begin{pmatrix} 1-\lambda^2/2 & \lambda & \lambda^3 A(\rho - i\eta) \\ -\lambda & 1-\lambda^2/2 & \lambda^2 A \\ \lambda^3 A(1-\rho-i\eta) & -\lambda^2 A & 1 \end{pmatrix}$$

The fact that one of the parameters can be imaginary allows for so called "natural" CP violation in the standard model. One of the unitarity conditions for the CKM matrix reads:

$$V_{ud}V_{ub}^* + V_{cd}V_{cb}^* + V_{td}V_{tb}^* = 0,$$

or

$$\frac{V_{ub}^*}{|\lambda V_{cb}|} + \frac{V_{td}}{|\lambda V_{cb}|} = 1$$

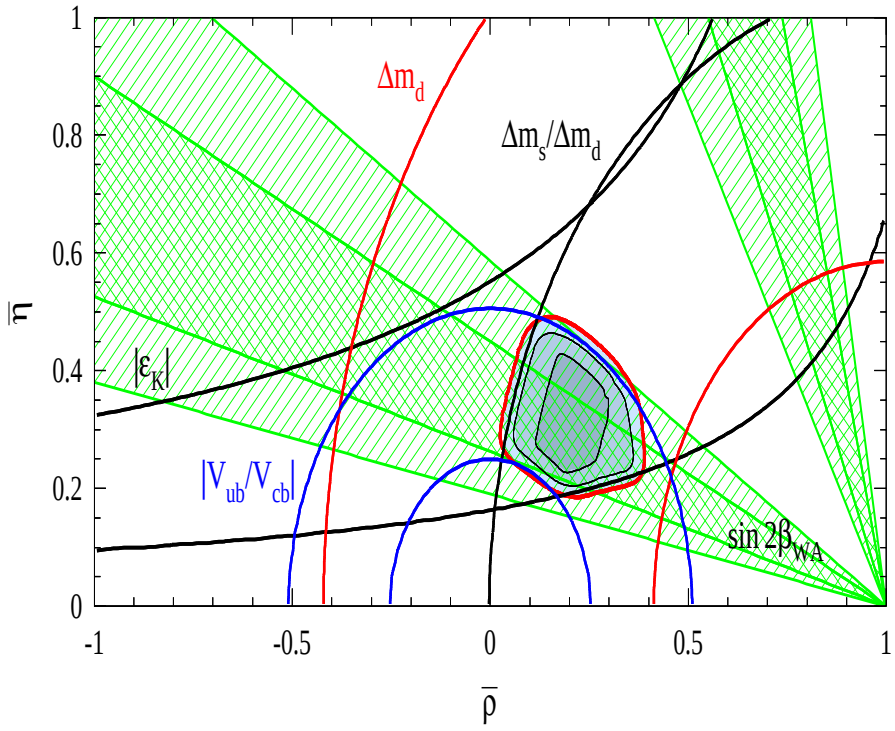


Figure 1.2: *Latest constraints on the vertex of the Unitarity triangle in the* $(\eta, \rho)$ *plane.*

The last relation is expressed as a triangle on a $(\rho, \eta)$ plane (see Fig. 1.1). It is referred to as the Unitarity Triangle. The fact that it is a triangle itself indicates that we have three generations of quarks. The constraints on the sides of the triangle come from measurement of B mixing and semileptonic decays. These together with the recently obtained angle $\beta$ constraint now limit the position of the tip of the triangle to the shaded area shown in Figure 1.2. If CP were not violated then the tip would be on the $\rho$ axis, i.e., $\eta = 0$.

## 1.3 CP Violation in the B System

Let's now consider B mesons. As we can infer from the form of (1.2.1) the mass eigenstates $|B_L\rangle$ and $|B_H\rangle$ are mixtures of the flavor eigenstates $|B^0\rangle$ and $|\overline{B}^0\rangle$:

$$|B_L\rangle = p|B^0\rangle + q|\overline{B}^0\rangle$$
$$|B_H\rangle = p|B^0\rangle - q|\overline{B}^0\rangle. \tag{1.3.1}$$

and vice versa,

$$|B^0\rangle = \frac{1}{2p}(|B_H\rangle + |B_L\rangle)$$
$$|\overline{B}^0\rangle = \frac{1}{2q}(|B_L\rangle - |B_H\rangle). \tag{1.3.2}$$

The fact that $|p| \neq |q|$ could result in a difference between the probability of $B^0$ to oscillate into $\overline{B}^0$ and the probability of $\overline{B}^0$ to oscillate to $B^0$. This is

one of the manifestations of so-called *indirect* CP violation, first discovered in K system [2]. For more information on CP violation please refer to [14] and [15].

## 1.4 Time-dependent CP Asymmetry

The difference between the masses of the heavy and light $B_d$ meson flavor, $\Delta m_{B_d}$, is measurable [29],

$$x_d \equiv \Delta m_{B_d}/\Gamma_{B_d} = 0.73 \pm 0.05.$$

However, the difference of the lifetimes of the two neutral $B_d$ mesons is very small[3] [4],

$$\Delta\Gamma_{B_d} = \Gamma_H - \Gamma_L \ll \Gamma_{B_d},$$

and therefore,

$$\Delta\Gamma_{B_d} \ll \Delta m_{B_d}.$$

Any B meson state can be written as an admixture of the states $B_H$ and $B_L$ with amplitudes that evolve in time:

$$a_H(t) = a_H(0)e^{-iM_H t}e^{-\frac{1}{2}\Gamma_H t},$$
$$a_L(t) = a_L(0)e^{-iM_L t}e^{-\frac{1}{2}\Gamma_L t}. \qquad (1.4.1)$$

A state that at time $t = 0$ is created as pure $B^0$ or $\overline{B}^0$ is denoted as $|B^0_{phys}\rangle$ or $|\overline{B}^0_{phys}\rangle$ correspondingly. For these states from 1.4.1 and 1.3.2:

[3] According to the recent hypotheses this might not be valid for $B_s$ mesons [16].

$$|B^0_{phys}\rangle = g_+(t)|B^0\rangle + (q/p)g_-(t)|\overline{B}^0\rangle,$$
$$|\overline{B}^0_{phys}\rangle = (q/p)g_-(t)|B^0\rangle +, g_+(t)|\overline{B}^0\rangle, \tag{1.4.2}$$

where

$$g_+(t) = e^{-iMt}e^{-\frac{1}{2}\Gamma}cos(\Delta m_B t/2),$$
$$g_-(t) = e^{-iMt}e^{-\frac{1}{2}\Gamma}i \cdot sin(\Delta m_B t/2). \tag{1.4.3}$$

At PEPII the $B^0$ and $\overline{B}^0$ mesons produced from the decay of the $\Upsilon(4s)$ are in a coherent $L = 1$ state. This means that they evolve in phase according to (1.4.1) and (1.4.2). Therefore, until one particle decays, there is exactly one $B^0$ and one $\overline{B}^0$ meson present. Let's assume that at some point in time, $t_{tag}$, one of the $B$ mesons decays into some final state $f_{tag}$ that is characteristic for the particular b-flavor. This implies that at $t_{tag}$ the other $B$ meson must be of the opposite b-flavor. This important characteristic of quantum correlated state of two particles was first described by A. Einstein, B. Podolsky and N. Rosen [11]. Now let's assume that the second $B$ meson, whose flavor was identified at $t_{tag}$, decays to the CP eigenstate $f_{CP}$ at some point in time - $t_{CP}$. If $R(t_{tag}, t_{CP})$ is the rate of this two-step process then the CP violation in B system would imply that the CP violation amplitude $a_{f_{CP}}$ is non-zero:

$$a_{f_{CP}} = \frac{R(t_{tag}, t_{CP}) - R(t_{anti-tag}, t_{CP})}{R(t_{tag}, t_{CP}) + R(t_{anti-tag}, t_{CP})} \neq 0, \tag{1.4.4}$$

where $anti - tag$ denotes the opposite flavor.

From (1.4.2) one can derive the expression for $R(t_{tag}, t_{CP})$ and then substitute it in (1.4.4) to obtain (for details see [21]):

$$a_{f_{CP}} = \frac{(1 - |\lambda_{f_{CP}}|^2)cos(\Delta m_B t) - 2\Im m\lambda_{f_{CP}} sin(\Delta m_B t)}{1 + |\lambda_{f_{CP}}|^2}, \tag{1.4.5}$$

where $\lambda_{f_{CP}} \equiv \frac{q}{p}\frac{\overline{A}_{f_{CP}}}{A_{f_{CP}}}$, and $\overline{A}_{f_{CP}}, A_{f_{CP}}$ are amplitudes for a $\overline{B}^0$ or $B^0$ to decay to a final state $f_{CP}$.

As it can be seen from (1.4.5), CP violation is possible if one of the three conditions exists:

1. $|\lambda_{f_{CP}}| = 1$, but $\Im m\lambda_{f_{CP}} \neq 0$ - indirect CP violation between decays with and without mixing.

2. $\frac{q}{p} \neq 1$ - indirect CP violation in mixing (even if $A_{f_{CP}} = \overline{A}_{f_{CP}}$).

3. $|\frac{\overline{A}_{f_{CP}}}{A_{f_{CP}}}| \neq 1$ - direct CP violation.

For processes such that $|\lambda_{f_{CP}}| = 1$ expression (1.4.5) simplifies considerably (indirect CP violation):

$$a_{f_{CP}} = -\Im m\lambda_{f_{CP}} sin(\Delta m_B t). \tag{1.4.6}$$

Here, as well as in (1.4.5), $t = t_{f_{CP}} - t_{tag}$. In the Standard Model $sin\, 2\beta = \Im m\lambda_{f_{CP}}$, where $\beta$ is one of the angles of the Unitarity Triangle, Figure 1.1. It is critical to note that the time-integrated value of the CP violation is zero in this case due to the term $sin(\Delta m_B t)$. This is why it is necessary to measure the time-dependence of $a_{f_{CP}}$ to measure indirect CP violation. This

is the effect that has been measured by the *BABAR* and Belle collaborations in July 2001. However, smaller CP violating effects (direct CP violation) for which $|\lambda_{f_{CP}}| \neq 1$ can be measured independent of time. It is estimated to be three orders of magnitude smaller than the indirect CP violation and that is why it is so hard to measure.

## 1.5 Inclusive $B\overline{B}$ Decays to Kaons

This section discusses motivation for the study of inclusive $B\overline{B}$ decays to kaons presented in this thesis. Although there is no direct experimental result that contradicts the Standard Model, there are several phenomena that are poorly described by it: certain discrepancies require complicated corrections or assumptions based upon debated results. Further in this section we will present two such puzzles and suggest the simple explanation involving "new physics" processes that can be found by studying $B \to K^0/\overline{K}^0 X$ decays.

One of the historical discrepancies between weak interaction phenomenology and the Standard Model is the $\Delta I = 1/2$ rule in $K \to \pi\pi$ decays. (Here $I$ denotes the isospin and $\Delta I$ is the change of the isospin in $K \to \pi\pi$ transition.) An S-wave two-pion state can have total isospin 0 or 2 and experimentally the $\Delta I = 1/2$ transition amplitude is larger than the $\Delta I = 3/2$ transition amplitude by a factor of twenty. In the Standard Model, however, this ratio is closer to $\sim 10$. More evidence of the discrepancy between existing measurements and the Standard Model appears in the semileptonic branching ratio of B mesons. Experimentally $Br_l(B) \sim 10 - 11\%$ [29], whereas the

parton model gives $Br_l(B) \geq 13\%$ [27].

These two outstanding discrepancies between the Standard Model and the experimental data lead to a hypothesis that chromomagnetic dipole operators due to new physics at the TeV scale may hold the solution [26]. (The chromomagnetic dipole operator is an analogy to the QED dipole operator for the strong interaction.)

Enhanced chromomagnetic dipole operators may explain not only these historical differences but also some newer effects seen in B physics such as the "charm deficit"[4] and the excess of kaons [25], because underlying new physics processes that enhance chromomagnetic dipole transitions such as $b \rightarrow sg$[5] should decrease $b \rightarrow charm$.

The topic of this thesis is the decay of the B meson into kaons, and in particular $K^0_S$. To date the ARGUS collaboration has presented the most precise measurement of $\mathrm{Br}(B\overline{B} \rightarrow K^0_S X)$ [23]. From this measurement one obtains the total number of $K^0$ mesons per B decay to be $Br(B\overline{B} \rightarrow K^0 X) = 64 \pm 4\%$. The sum of all known modes producing $K^0$ from b quarks through charm is $Br(B\overline{B} \rightarrow Charm \rightarrow K^0 X) = 59.4 \pm 5.6\%$ [26]. The excess of neutral kaons, if any, may be due to the enhanced $b \rightarrow sg$ [1]. The new physics chromomagnetic dipole operators at TeV scale can result in a branching fraction for $b \rightarrow sg \sim 10\%$. This is in contrast with the Standard Model predictions for $\mathrm{Br}(b \rightarrow sg) \sim 0.2\%$ [24].

[4]Current measurements of inclusive B decays to charm fall $\sim 20\%$ short of theoretical predictions.

[5]g denotes a gluon.

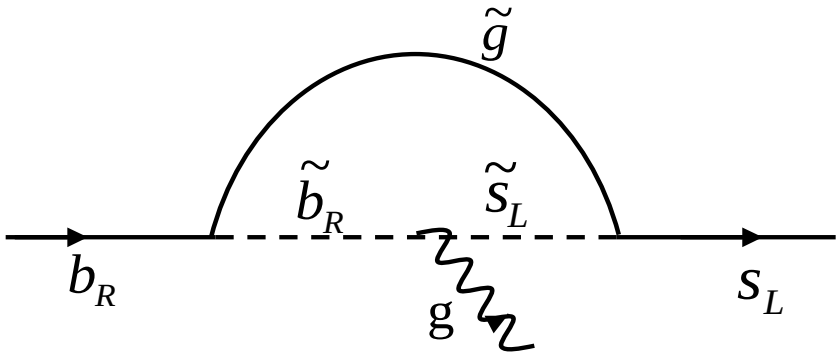


Figure 1.3: *The Supersymmetric gluino penguin graph.*

The chromomagnetic dipole operator for $b \to sg$ has a form:

$$Q_G^{sb\pm} = g_s \overline{s} \sigma_{\mu\nu} t^a \frac{1 \pm \gamma_5}{2} b G_a^{\mu\nu} \tag{1.5.1}$$

Most generally the corresponding Lagrangian terms:

$$\Delta L_G = \ldots + \sum_{i=+,-} C_G^{sbi}(\mu) Q_G^{sbi}(\mu) + H.c. + \ldots, \tag{1.5.2}$$

where coefficients C have dimension $(mass)^{-1}$ and $\mu$ is the renormalization constant.

An example of a "new physics" chromomagnetic dipole operator is the Supersymmetric gluino penguin. It is illustrated in Figure 1.3.

The mass contributions, obtained by removing gluons from the dipole graphs, are (this concept is illustrated in Figure 1.4):

$$\Delta L_{mass} = \ldots + \Delta m_{sb}^{+} \overline{s}_L b_R + \Delta m_{sb}^{-} \overline{s}_R b_L + H.c. + \ldots, \tag{1.5.3}$$

Comparing (1.5.2) and (1.5.3), the dipole operator coefficients then are:

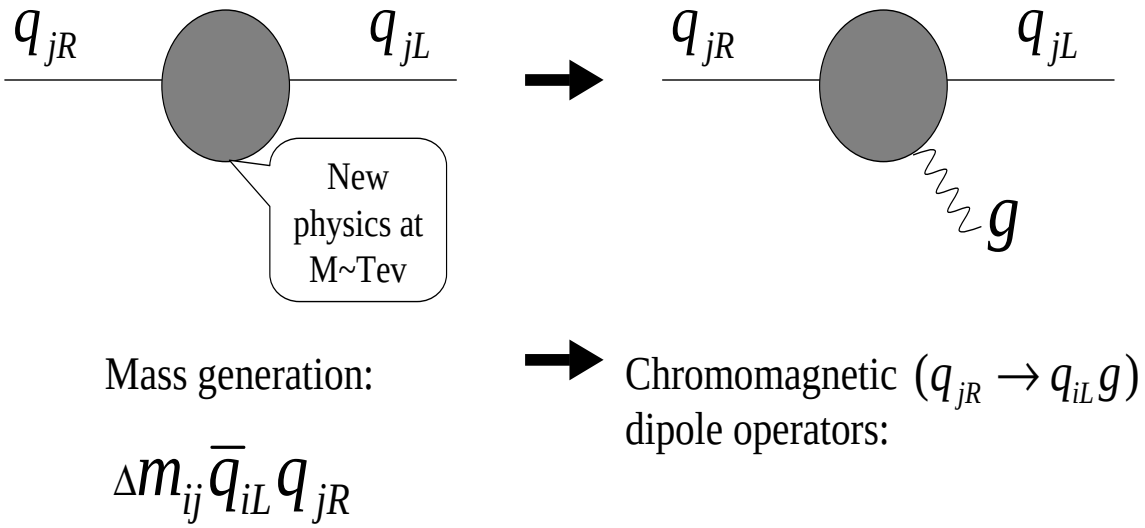


Figure 1.4: *A Scheme taken from presentation of Alexander L. Kagan given at SLAC.*

$$C_G^{sb\pm}(\mu) = \eta(\mu)\zeta_G \frac{\Delta m_{sb}^{\pm}(M)}{M^2} \qquad (1.5.4).$$

Here $M$ is the scale of the new physics and $\zeta_G$ is a dimensionless constant of order of one. Equations (1.5.2), (1.5.3) and (1.5.4), given the measured masses of the quarks and CKM matrix elements, predict that $\mathrm{Br}(b \to sg)$ $\sim 10\%$ for a scale of the new physics at about $M \sim 1TeV$.

The inclusive charged kaon, unlike neutral kaon, branching fractions have been measured with comparatively good accuracy by both ARGUS and CLEO [23], [28]. The values are approximately $3\sigma$ to $3.5\sigma$ in excess of

the corresponding kaon yields from $B \to X_c \to KX$ decays[6]:

$$Br(B \to K^+/K^-X) - Br(B \to X_c \to K^+/K^-X) = (0.178 \pm 0.053) \quad (1.5.5)$$

This suggests that the charmless $b \to s$ decay rate may indeed be an order of magnitude larger than in the Standard Model. It also needs to be pointed out that $b \to sg$ seems to be the only phenomenologically viable possibility to account for the observed increased kaon yields [1].

The neutral kaon yields have been measured with worse precision.

$$Br(B \to K^0/\overline{K}^0X) - Br(B \to X_c \to K^0/\overline{K}^0X) = (0.046 \pm 0.069) \quad (1.5.6)$$

The equation (1.5.6) for the case of neutral kaons does not show clear excess. Better measurements are thus necessary.

The Particle Data Group value [29] (essentially the ARGUS' result since CLEO has not updated its almost fifteen year old result) needs to be more precise in order to make any conclusions about the excess of inclusive $K_0$. I have decided to make a new measurement of inclusive $K_0$ coming from $B\overline{B}$ using BABAR data. Taking into account all mentioned above, it looks like an interesting topic that can have potentially very important implications. The particular yield that I am going to measure is $B\overline{B} \to XK^0_S \to \pi^+\pi^-$.

The predicted spectrum of the $K^0_S$ due to the enhanced $b \to sg$ is shown in Figure 1.5.

[6]Here, $X_c$ stands for some charmed state.

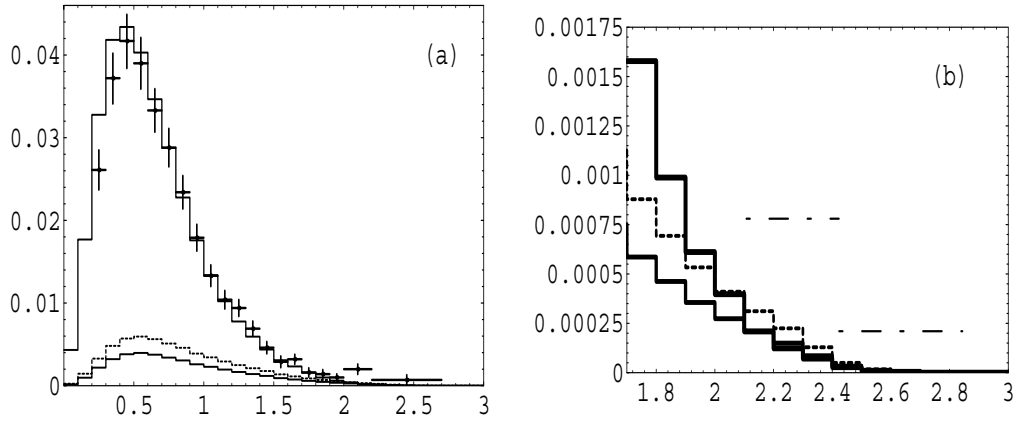


Figure 1.5: $\mathcal{B}(B \to K_s X)$ *vs.* $p_{K_s}$ *[GeV]. Branching ratios are for* 0.1 *GeV bins except CLEO upper limits. (a) ARGUS data (crosses), Monte Carlo (top solid), Monte Carlo for* $\mathcal{B}(\overline{B} \to X_{sg}) = 10\%$ *with* $p_F = 250$ *MeV (bottom solid) and* $p_F = 0$ *(dashed). (b) fast kaon spectra: CLEO 90% CL UL's for* $2.11 < p_{K_s} < 2.42$, $2.42 < p_{K_s} < 2.84$ *(dot -dashed), SLD Monte Carlo (thick solid), Monte Carlo for* $\mathcal{B}(\overline{B} \to X_{sg}) = 10\%$ *with* $p_F = 250$ *MeV (solid) and* $p_F = 0$ *(dashed).*

# Chapter 2

# The $BABAR$ Detector

## 2.1 Introduction

The existence of b quark was predicted by Kobayashi and Maskawa quite ahead of its time in 1973 [3]. Then followed the discovery of $\Upsilon(1S)$, $\Upsilon(2S)$ and $\Upsilon(3S)$ resonances in 1977-1978. These new and exciting results fueled the interest in B physics and in 1983 B mesons were finally discovered by the CLEO I collaboration at the Cornell Electron Storage Ring(CESR). B mesons were produced at the $\Upsilon(4S)$ resonance, the first $b\overline{b}$ resonance that lies above $B$ meson threshold. One indication of this is that its width is significantly larger than the widths of $\Upsilon(1S)$, $\Upsilon(2S)$ and $\Upsilon(3S)$, see Figure 2.1. From $\Upsilon(4S)$ only $B_d$ mesons are produced and to see $B_s$ mesons it is necessary to produce the heavier $\Upsilon(5S)$ resonance. CESR operated as a symmetric $e^+e^-$ collider and that made it impossible for CLEO to measure CP violation in B system, since the very nature of this phenomenon in B sys-

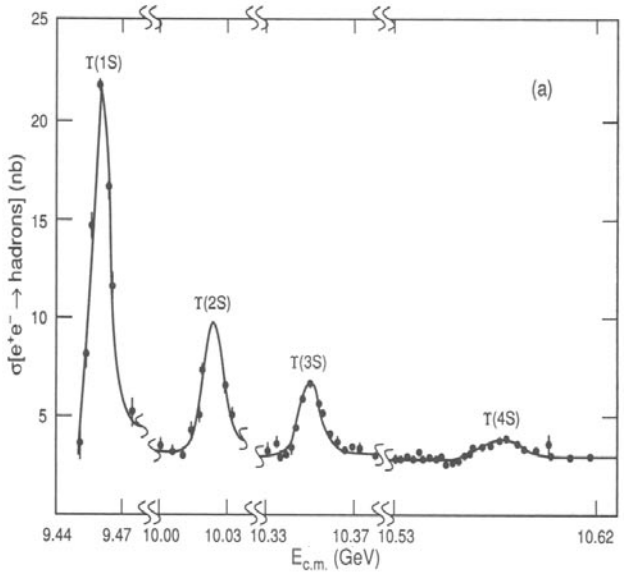


Figure 2.1: *The Upsilon resonances.*

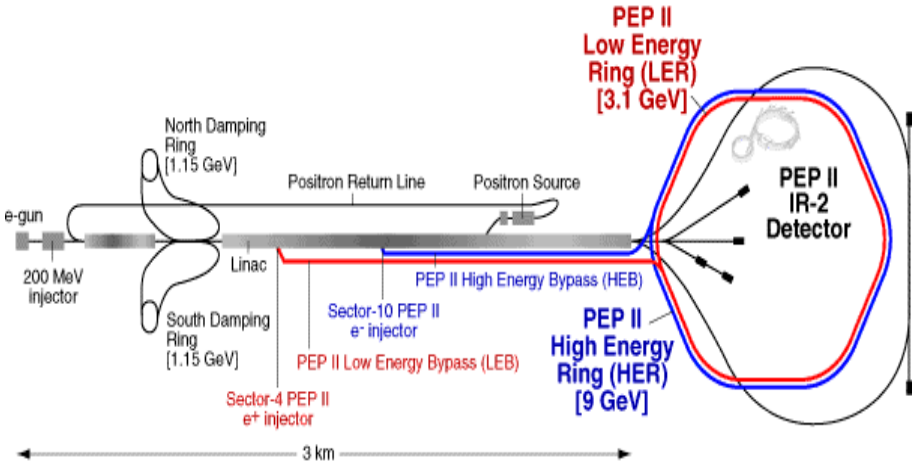


Figure 2.2: *The PEPII shown schematically.*

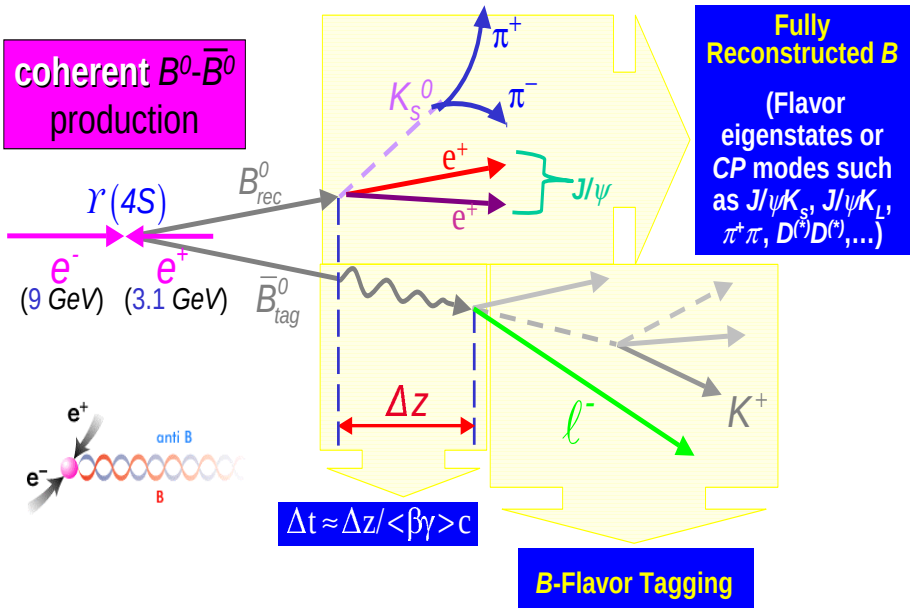


Figure 2.3: *Schematic view of the flavor tagged CP violating $B\overline{B}$ decay. Sufficient $\Delta z$ separation between "tag" B and CP violating B decays is necessary to measure the time difference.*

tem requires precise measurement of the times of the decays of the $B\overline{B}$. At a symmetric collider $\Upsilon(4S)$ resonances, and hence B mesons, are produced at rest in the lab frame and this makes it impossible to measure the difference of the positions of decay vertices of B mesons - the information necessary for CP violation measurement. Unlike CLEO, at *BABAR* the electron beam has energy of 9 GeV and the positron beam - 3.1 GeV (Schematic view of the PEPII machine is shown in Figure 2.2). This results in the $\Upsilon(4S)$ resonance and B mesons to be produced moving with respect to the lab frame - $E_{CM} = M(\Upsilon(4S)) = 10.58\,GeV$. The $\beta\gamma$ of the B mesons is 0.56 in the lab frame and, despite the short lifetime, the average distance between B meson decay vertices in this case is detectable. This characteristic is very important for a time-dependent CP-violation measurement. It is because the time difference between the B meson decays is reconstructed by measuring their decay vertices separation which is larger and easier to measure with large $\beta\gamma$ of the B mesons. Figure 2.3 schematically shows the $B\overline{B}$ decays vertices separated due to the lab frame boost. (Time-dependent CP asymmetry was discussed in detail in the Chapter 1).

Soon after the B meson discovery, the four experimental conditions to measure CP violation have been understood [17], [18]:

1. An Asymmetric Collider is needed to be able to measure time-dependent CP asymmetry.

2. A Silicon Vertex Detector capable of resolution better than $\sim 0.25\,mm$ to be able to distinguish two B vertices.

3. The $B\overline{B}$ pairs need to be produced in a quantum correlated state, for example through $\Upsilon(4S)$. This condition is needed to tag the flavor of both B mesons at the moment of their decays.

4. The flavor of the B mesons decaying into a CP eigenstate final state needs to be determined via observation of the second B meson that serves as a "tag" in this case.

SLAC and KEK are asymmetric electron-positron beam machines that satisfy these conditions and BaBar and Belle are the experiments that are carried out on them respectively. *BABAR* announced the measurement of the CP violation in the B system on July 5, 2001 [12], followed by Belle on July 18 [13].

The two main tracking devices at the *BABAR* detector are the Silicon Vertex Tracker(SVT) and the Drift Chamber[1]. The charged particles traveling through those detectors leave hits that are reconstructed into tracks. The tracks are then fitted by fitting and vertexing algorithms. Neutral particles such as photons and some $K_L^0$ are detected by the Electromagnetic Calorimeter(EMC). (The $K_S^0$ is also a neutral particle but it decays usually within the SVT or the Drift Chamber and almost never reaches the EMC.) The $K_S^0$ is a light strange meson that consists of the combination of $s$ and $d$ quarks[2], whose two main decay channels of are $\pi^+\pi^-$ and $\pi^0\pi^0$: $BR(K_S^0 \to \pi^+\pi^-) = (68.61 \pm 0.28)\%, \quad BR(K_S^0 \to \pi^0\pi^0) = (31.39 \pm 0.28)\%$

[1]Further in this chapter the subsystems are described in detail.

[2]Just like in the case of B mesons (see the chapter 1.3), flavor eigenstates $K^0(d\overline{s})$ and $\overline{K^0}(\overline{d}s)$ are the mix of mass eigenstates $K_S^0$ and $K_L^0$.

[29]. $K_S^0$ decaying to charged pions can be reconstructed and vertexed to form the $K_S^0$ decay vertex, and its momentum can also be obtained by combining the reconstructed momenta of the pions. The above method lies at the foundation of the vertexing algorithm used in the $K_S^0$ analysis described in this thesis. Further in this chapter the essential subsystems of *BABAR* detector are discussed in detail.

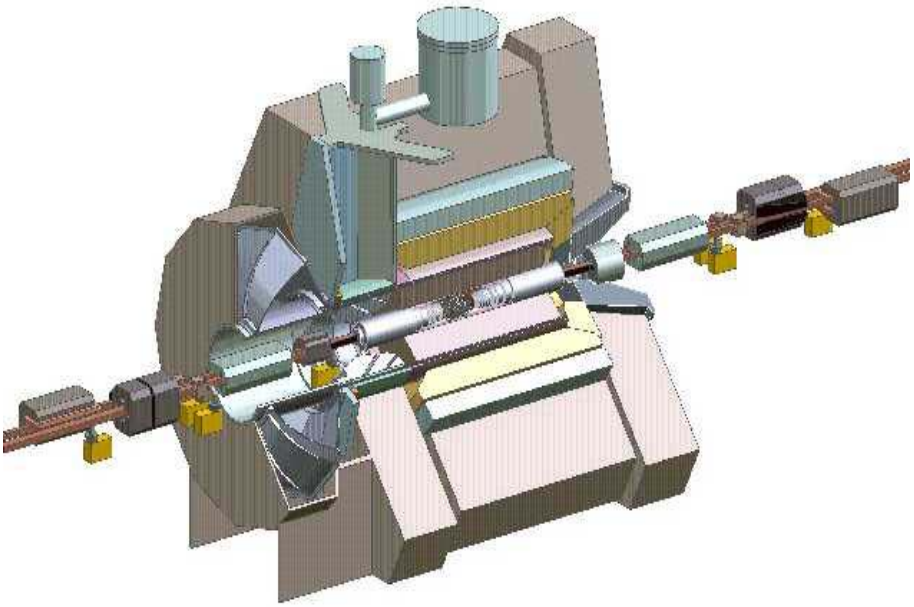

Figure 2.4: *The view of the BABAR Detector.*

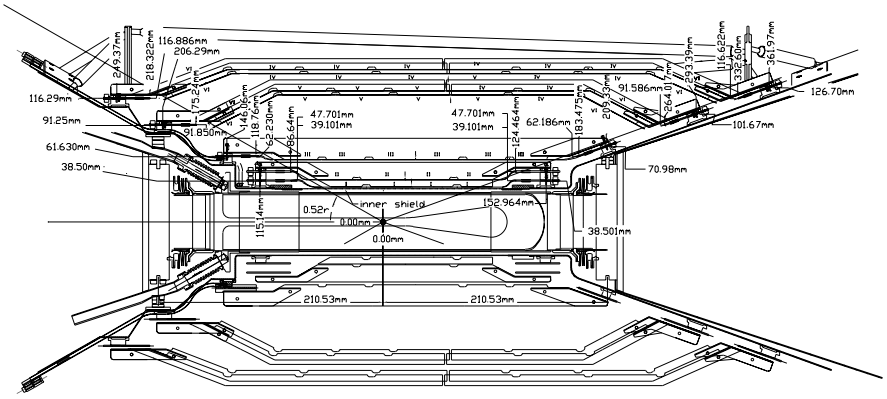


Figure 2.5: *The SVT.*

## 2.2 The Silicon Vertex Tracker

To measure time-dependent CP asymmetries in $B^0$ decays it is necessary to have sufficient time resolution of the two primary B meson vertices. Therefore the Silicon Vertex Tracker must allow the determination of two primary B meson vertices, for which the mean separation is $250\,\mu$m (see Figure 2.3).

Measuring the distance between two decay points we can obtain the time difference between the CP violating decay and the tag decay[3]. The precision requirement for this measurement translates into single vertex precision of better than $80\,\mu$m. The Silicon Vertex Tracker is designed to achieve the best practicable resolution which is limited by the multiple scattering. For inner layers it is 10-15 $\mu$m, and 30-40 $\mu$m for outer layers.

The Silicon Vertex Tracker also provides the only tracking information

[3]Considering the case of one B decaying in the tagging channel and the other into CP violating channel.

for charged tracks with low $p_t$. For example, tracks with $p_t$ lower than 100 MeV/c do not reach the Drift Chamber, and the Drift Chamber itself reaches full reconstruction efficiency only for tracks with $p_t$ higher than about 180 MeV/c. For this reason it is called Silicon Vertex Tracker rather than Silicon Vertex Detector.

Generally, the SVT needs to cover as much solid angle as possible. Since PEP-II is an asymmetric collider the coverage of the forward region is especially important. The SVT is designed to cover the polar angle between $20.1^0$ and $150.2^0$. It consists of five cylindrical layers of double sided silicon detectors: three inner barrel shaped layers and two outer layers that have arched barrel shape. See Fig 2.5.

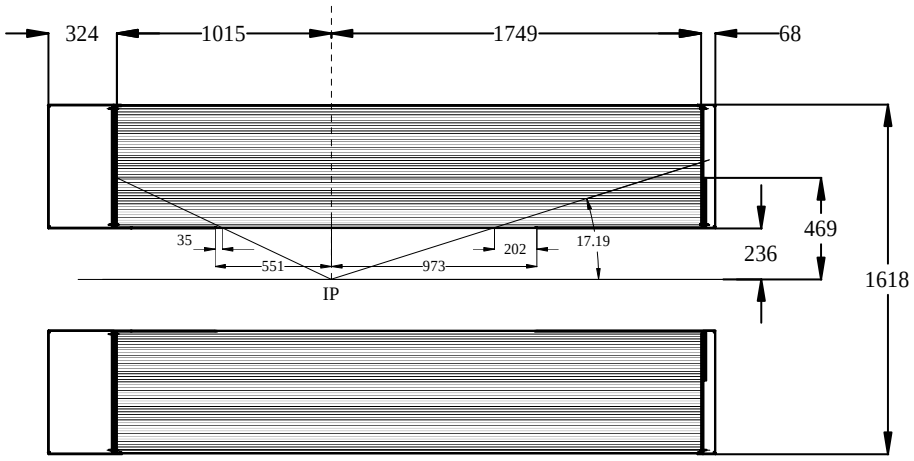


Figure 2.6: *The Drift Chamber.*

## 2.3 The Drift Chamber

The Drift Chamber(DCH) is the centerpiece of the BABAR detector. It is the main tracking device and the information it provides is essential in almost every physics measurement. The Drift Chamber Trigger is also designed to be one of the principal triggers in the experiment. The DCH provides up to 40 spatial measurements per track for tracks with $p_{\mathrm{t}}$ greater than 100 MeV/c. The position resolution on the average is better than 140 $\mu$m in the $R-\phi$ plane. In addition, The Drift Chamber supplies the Particle Identification for low momentum[4] tracks, measuring $\frac{dE}{dx}$ with a resolution of 7%.

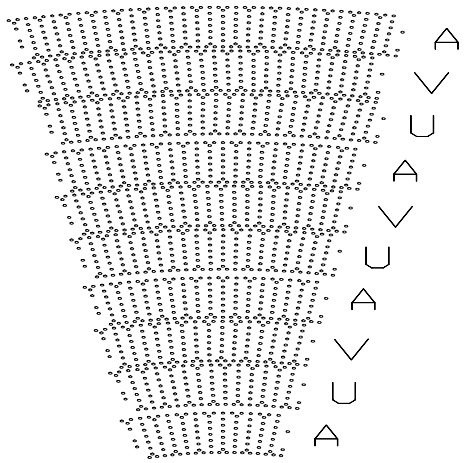

Figure 2.7: *Cell layout in the Drift Chamber.*

The Drift Chamber consists of two concentric cylinders of radii 23.6 cm and 80.9 cm. The inner cylinder is made from 1 mm beryllium to achieve minimal radiation loss while being conductive and sturdy[5]. It is important

[4]Below 700 MeV/c.

[5]1 mm of beryllium corresponds to 0.28 percent of the radiation length.

to isolate the tracking volume of the DCH from external electromagnetic background. This is why both the inner and the outer cylinders are made conductive. The outer cylinder consists of two layers of carbon fiber on a Nomex core with conductive foil glued on the top. The backward endplate is made from 24 mm thick aluminum and it supports all the read-out electronics modules. The forward endplate is also made from 24 mm thick aluminum but the portion of it in the detector acceptance region is made to be twice as thin in order to minimize the matter in front of the forward EMC crystals (see Fig 2.6). In the inner region 28768 wires are strung to form 10 superlayers of 4 layers each, for a total of 40 cell layers with the total number of cells 7104. The axial (A) and stereo (U,V) superlayers alternate as shown in Fig 2.7. The Drift Chamber utilizes an 80:20 Helium:isobutane gas mixture to obtain good resolution while minimizing the material.

The Princeton University group had primary responsibility for construction, commissioning and operation the Drift Chamber.

## 2.4 The DIRC

The DIRC, or Detection of Internally Reflected Cherenkov (light), is a new type of detector that uses Cherenkov radiation to identify particles. Unlike the traditional ring-imaging Cherenkov counters, the DIRC collects the photons trapped in the radiator due to total internal reflection. The Radiator consists of 144 long straight bars of synthetic quartz arranged in a 12-sided polygonal barrel, see Fig 2.8. The internally reflected light is passed

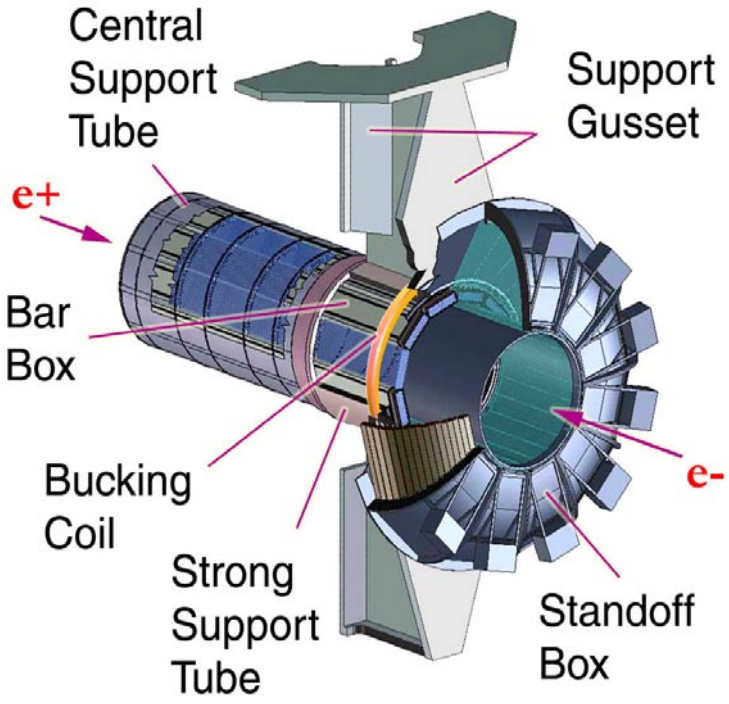


Figure 2.8: *Schematic of DIRC mechanical elements.*

in the backward direction where it is allowed to expand in the the Stand-off Box(SOB). (The Schematic path of the Cherenkov photons is shown in the Figure 2.9.) The SOB is filled with purified water with the refractive index close to that of quartz[6] so that the reflection at the water-quartz surface is small. Finally, the Cherenkov photons are detected by 11000 2.5 cm photomultipliers.

Only tracks with $p_t$ larger than 250 MeV/c reach the DIRC. The Radiator covers 87% of the polar solid angle and 93% in $x - y$ plane.

[6]refractive index of quartz is 1.474 and of water - 1.33

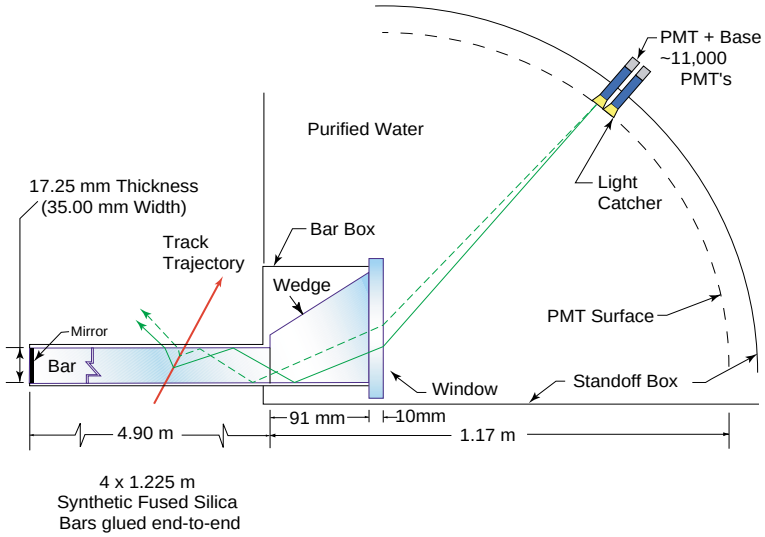


Figure 2.9: *Schematic view of the Cherenkov photon path in the DIRC.*

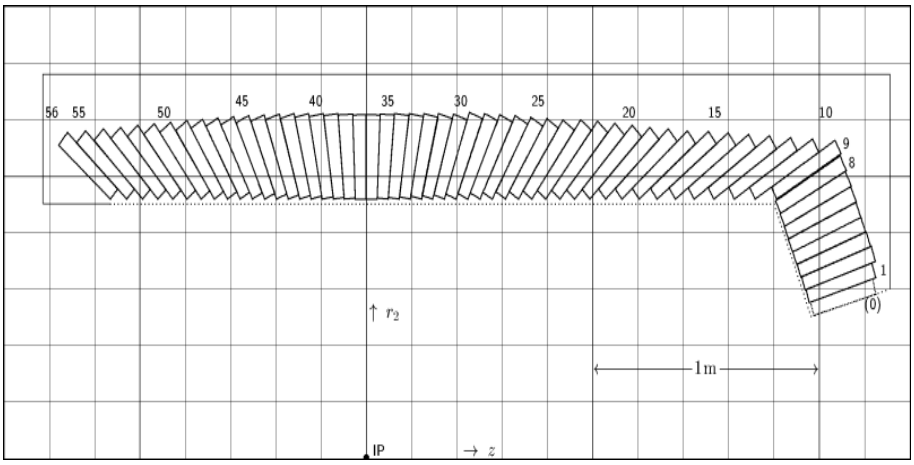


Figure 2.10: *Schematic r-z view of the calorimeter.*

## 2.5 The Electromagnetic Calorimeter

The Electromagnetic Calorimeter design is based on quasi-projective CsI(Tl) crystals. It consists of a cylindrical barrel and conical endcap. The barrel

part of the calorimeter consists of 5760 crystals positioned in 48 polar angle rows, each having 120 crystals in azimuthal angle. The crystals are grouped in 280 modules that are made from 300 $\mu$m thick carbon fiber composite (CFC) material and held from the rear by an aluminum strongback. They are mounted in an aluminum support cylinder, which in turn is fixed to the coil cryostat. By supporting the crystals from the rear, minimal material is placed in front of them. The EMC front material consists of two 1 mm thick cylinders of aluminum, separated by foam, which provide a gas seal and RF shielding. Additional front material due to a liquid radioactive source calibration system consists of the equivalent of another 3 mm of aluminum. Cooling, cables, and services are located at the back of each module and thus do not add to the inactive-materials budget. The forward endcap is a section of a cone. It currently consists of 820 CsI(Tl) crystals.

## 2.6 The IFR

The instrumented flux return (IFR) is the subdetector consisting of Resistive Plate Chambers (RPCs) filling the space in between plates of the laminated magnet yoke[7]. The main purpose of IFR is the detection of muons as well as neutral hadron detection such as $K_L^0$.

At the $\Upsilon(4S)$ muons are produced mostly in semileptonic decays either directly from the B mesons or from the cascade $D_s$. The sign of the charge determines the b or c flavor of the parent meson, thus providing a tag for

[7]Huge iron structure in hexagonal shape surrounding the detector.

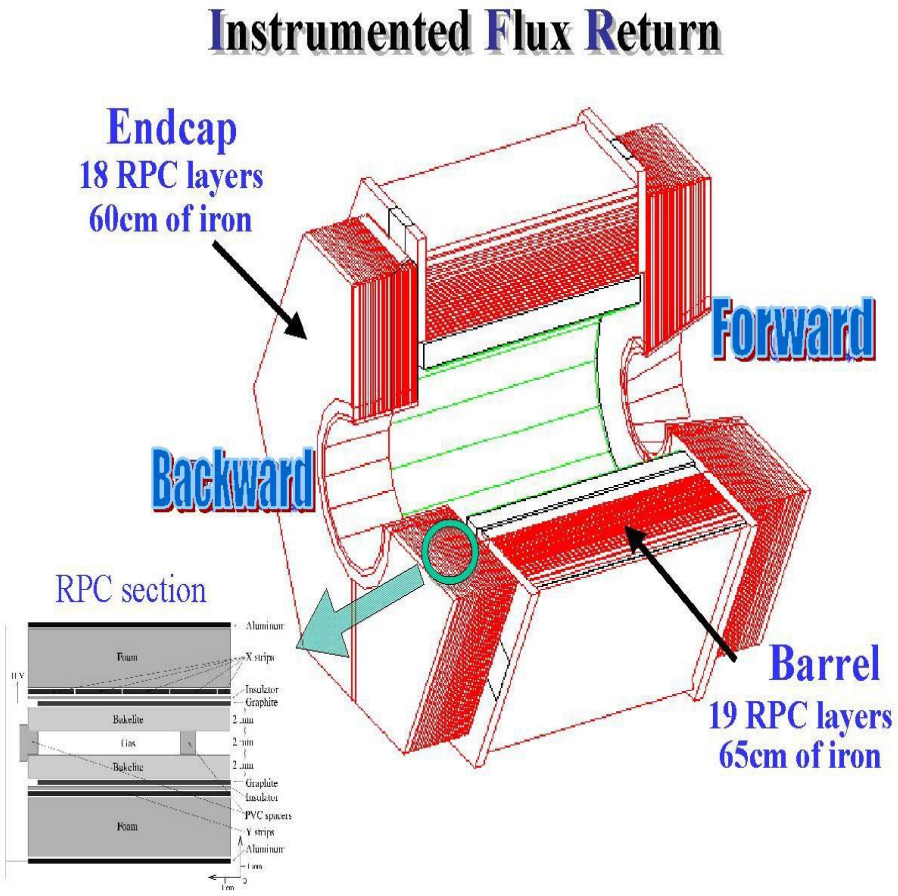


Figure 2.11: *Schematic of the IFR layout.*

the CP asymmetry measurements. The main goal for the IFR detector is to achieve the highest practical tagging efficiency. Muon selection efficiency is up to 90% with the fake rate, or the rate of identifying another particle as a kaon, of $\sim 5\%$. The $K_L^0$ efficiency is $\sim 30\%$. For schematic view of the IFR detector please see 2.11.

## 2.7 The Trigger

The BaBar Trigger performs selection of the events observed by the BaBar detector. It is designed to choose which events are interesting enough to keep and record, and then be later analyzed for physics content.

The trigger system at *BABAR* consists of two levels: Level 1 trigger and Level 3 trigger[8]. Level 1 trigger is designed to execute at the hardware level and it consists of the four main components: the charged particle trigger (the Drift Chamber Trigger), the neutral particle trigger (the Electromagnetic Calorimeter Trigger), the cosmic trigger (the Instrumented Flux Return Trigger) and the Global Level Trigger (GLT). The charged track trigger requires at least two tracks in the drift chamber: one long track with $p_{\rm t} > 0.18\,{\rm GeV/c}$ and one short track with $p_{\rm t} > 0.12\,{\rm GeV/c}$. The neutral particle trigger requires two energy deposits in the electromagnetic calorimeter. Nominally, the Level 1 trigger output rate is below 1.5 kHz and simulation indicates that it is 100% efficient for $B$ and $\tau$ physics (i.e. events where B or $\tau$ are produced initially) and more than 99% efficient for $\gamma\gamma$ physics.

Level 3 trigger is the combination of software tools designed to reduce the background rates while preserving the physics. Nominal output rate of the Level 3 trigger is around 100 Hz.

[8]The choice of the name of the Level 3 trigger was made to accommodate an additional intermediate level of the trigger - Level 2 - should it become necessary.

# Chapter 3

# Analysis of inclusive $B\overline{B}$ decays to $K^0_S$

## 3.1 Introduction

This chapter presents a study of the inclusive branching fraction of B mesons decaying into $K^0_S$. The actual number measured is the number of $K^0_S$ mesons per B decay, i.e. multiplicity, and it is sometimes referred to as inclusive branching fraction for heavy particles. Hence the words branching fraction and multiplicity will be used interchangeably to refer to the same numerical fraction. The physics motivation showing the importance of the total number of neutral Kaons per B event was described in chapter 1. Previously this number was measured by the ARGUS collaboration, their result was: $0.64 \pm 0.04$ [23]. This thesis presents a new measurement of this value with the same overall uncertainty.

Also presented is the inclusive $K_S^0$ momentum spectrum. This is the number of $K_S^0$ mesons per B meson as a function of the $K_S^0$ momentum. Monte Carlo simulation is used to calculate the efficiencies in different momentum bins. Then these efficiencies are convoluted with the observed spectrum of $K_S^0$ to obtain differential multiplicities that are independent of efficiency. Previous measurement of the $K_S^0$ multiplicities is shown in Figure 3.1.

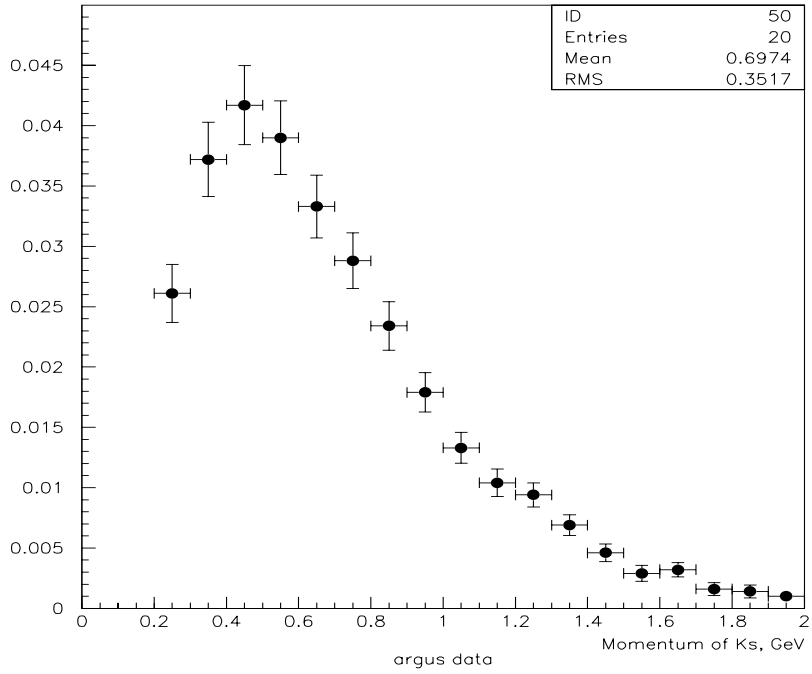


Figure 3.1: *$K_S^0$ multiplicity in B meson decays as a function of momentum. Argus Collaboration 1993.*

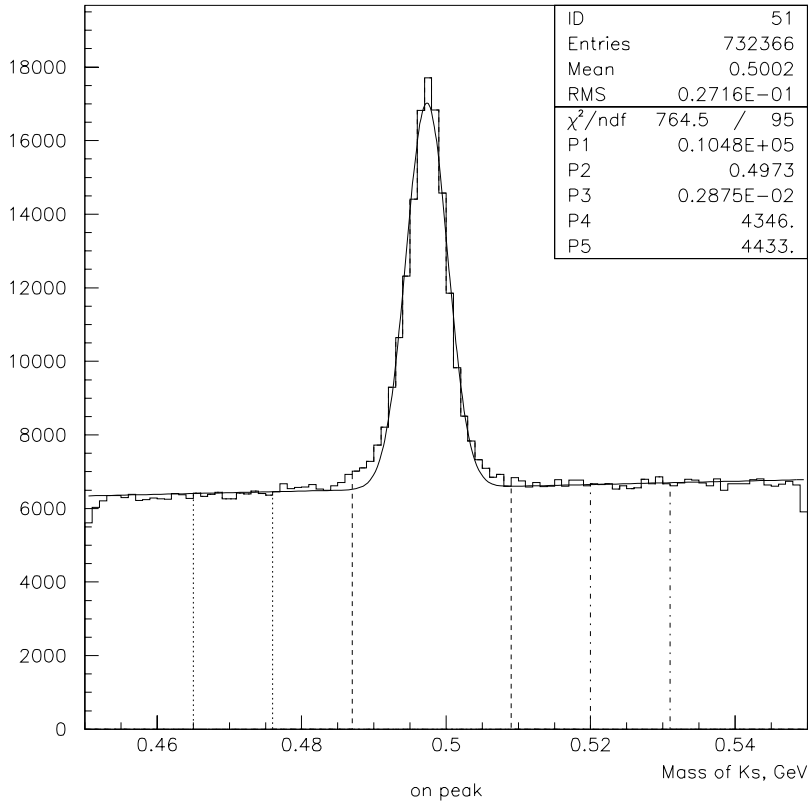


Figure 3.2: *Mass of the $K^0_s$s obtained with the data taken at the $\Upsilon(4S)$ center of mass energy - 10.58 GeV (on peak). Total luminosity of 156 $pb^{-1}$.*

## 3.2 Data analysis

$K^0_S$ are often produced in $B$ decays. On average, 100000 $B$ mesons produce 32000 $K^0_S$ mesons, and assuming a reconstruction efficiency of 25%, the analysis selects 8000 $K^0_S$. Therefore, a relatively modest amount of data of about $200\,pb^{-1}$ is sufficient to perform this analysis with a statistical precision that

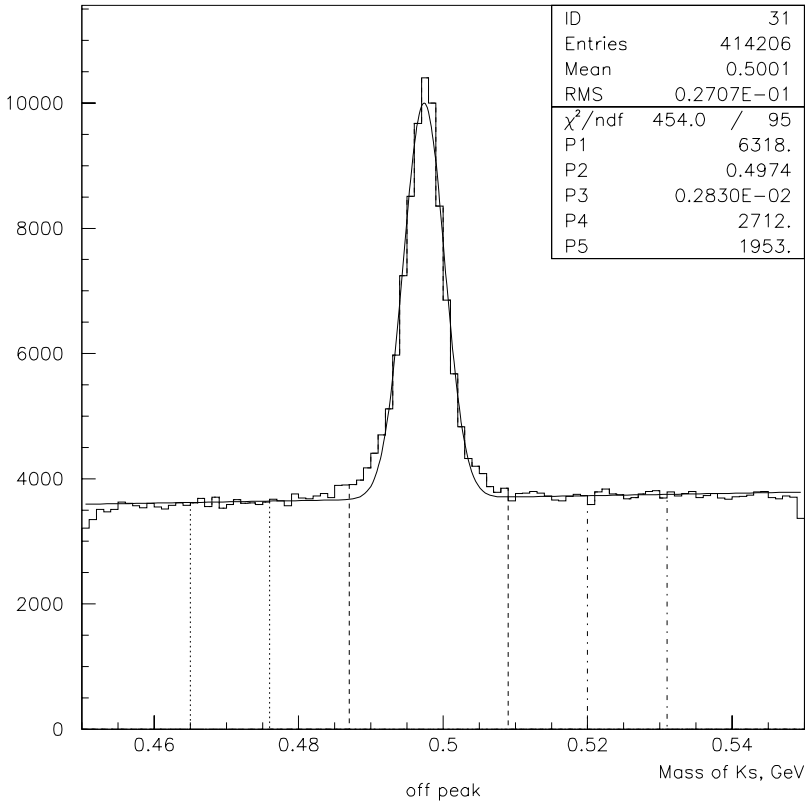


Figure 3.3: *Mass of the $K^0_s$s. Data was taken at the center of mass energy of 10.5398 GeV, i.e. ∼40 MeV bellow $\Upsilon(4S)$ peak (off peak). Total luminosity of 130 $pb^{-1}$.*

surpasses the previous ARGUS measurement. The data selected for use in this analysis was taken during the stable running in the end of the year 2000. To avoid possible discrepancies between several different samples of data due

to different detector or software configurations, the chosen runs[1] are taken within a limited period of time.

As discussed in chapter two, $B\overline{B}$ mesons are produced at *BABAR* through the decay of the $\Upsilon(4S)$ resonance, whose mass is 10.58 GeV. Therefore for the majority of runs PEPII collider beam center of mass energy is set at 10.58 GeV - this is called "on peak" running. However many analyses need the information about the interactions of particles at energies close but not quite equal to the $\Upsilon(4S)$ mass. For this reason, some of the runs are taken at the center of mass energy 10.54 GeV - "off peak" runs. The analysis presented in this thesis uses both on peak and off peak runs. As discussed below, the off peak sample is needed in particular to exclude the background.

The information about the selected on peak and off peak runs was obtained using one of the *BABAR* software analysis scripts called the Lumi script. For a given run number (or range of runs) this script returns the total luminosity of the data contained in the run. It also counts the numbers of $B\overline{B}$ and $\mu\overline{\mu}$ pairs. The latter number can be used as an additional tool for luminosity estimation thus providing a valuable cross check to the luminosity value itself that is counted via the estimation of the number of $\gamma\gamma$ pairs[2]. The information about the chosen runs is summarized in Tables 3.1 and 3.2.

These runs were analysed and the resulting $K^0_S$ mass peaks are shown in

[1] A run is an elemetary amount of data collected continuously during a short period of time ∼up to a few hours. Runs are numbered consecutively, indicating the order in time that they occured.

[2] The luminosity is calculated by measuring the rate of the production of $\mu\overline{\mu}$ or $\gamma\gamma$ and then dividing this rate by the corresponding known production cross-section.

| Information on the analysed data on peak | | | |
|---|---|---|---|
| run # | $\# \mu^+\mu^-$ | Lumi, $pb^{-1}$ | $\# B\overline{B}$ |
| 16575 | 6290±79 | 13.173 | 15324±468±245 |
| 16582 | 7924±89 | 15.974 | 17478±523±280 |
| 16584-16586 | 6601±81 | 13.333 | 14781±478±237 |
| 16593-16599 | 25721±160 | 52.813 | 59777±944±956 |
| 16608-16614 | 29648±172 | 60.362 | 66839±1012±1069 |
| Total | 76184±276 | 155.654 | 174199±1623±2787 |

Table 3.1: *Various information about the runs taken at the $\Upsilon(4S)$ center of mass energy, 10.58 GeV, that is available through the Lumi script [30] is presented in this table. Errors are systematic for $\#\mu^+\mu^-$ and statistical and systematic for $\#B\overline{B}$ respectively.*

Figures 3.2 and 3.3.

## 3.3 Reconstruction and Monte Carlo Simulation

The majority of physics results in B physics are obtained assuming that the $\Upsilon(4S)$ decays only to $B^+B^-$ and $B^0\overline{B}^0$ with the rate of 50% in each case. This assumption is justified because the rate of non-$b\overline{b}$ decays for $\Upsilon(4S)$ is negligibly small compared to $b\overline{b}$ decays [29]. That is why everywhere in this document it is implied that $\Upsilon(4S)$ decays to $bb$ with the rate of 100% and

| Information on the analysed data off peak | | |
|---|---|---|
| run # | number of $\mu^+\mu^-$ pairs, $\#\mu^+\mu^-$ | Lumi, $pb^{-1}$ |
| 16523-16525 | 1799±42 | 3.792 |
| 16527-16528 | 14953±122 | 31.205 |
| 16531 | 7785±88 | 16.030 |
| 16533 | 5091±71 | 10.485 |
| 16535-16539 | 33128±182 | 68.730 |
| Total | 62756±251 | 130.242 |

Table 3.2: *Presented is various information about the runs taken at the center of mass energy of 10.5398 GeV, i.e. off* $\Upsilon(4S)$ *peak. Errors for* $\#\mu^+\mu^-$ *are systematic.*

that $b\overline{b}$ pair decay rate to $B^+B^-$ and $B^0\overline{B}^0$ is equal to 50%.

*BABAR* Monte Carlo software generates $b\overline{b}$ pairs that then are allowed to decay through $B^+B^-$ and $B^0\overline{B}^0$ to all possible final states. Such, non-specific, events are called generic events and they are usually used in inclusive studies. Particularily, used for this study was a set of simulated generic $b\overline{b}$ events of the latest available version of simulation production called SP3. Both the data sample and the Monte Carlo have been analysed with the same software package versions. 100000 $b\overline{b}$ events in total have been generated and analysed with SP3 Monte Carlo.

Figure 3.4 shows the mass distribution of $K_S^0$ mesons selected by the analysis from the Monte Carlo sample. The efficiency of the reconstruction is obtained by counting the number of reconstructed $K_S^0$ candidates that passed the selection and dividing it by the number of $K_S^0$ mesons generated.[3]

There are several methods of counting the particles selected by the analysis. One is to fit the observed line shape of the particle candidate's mass distribution. In the simplest approximation a single Gaussian lineshape is assumed and then the number of particles selected can be found by calculating the area under the fit. In order to get a reliable estimate of the number of the candidates the functional shape of the mass peak needs to be known quite accurately. This is often difficult because of the differences in tracking parameters for candidates that had different physical characteristics, for example flight length or momentum. The masses of badly reconstructed

[3]The number of $K_S^0$ generated can be obtained from Monte Carlo tables, called the truth tables, where all the information about generated events is stored.

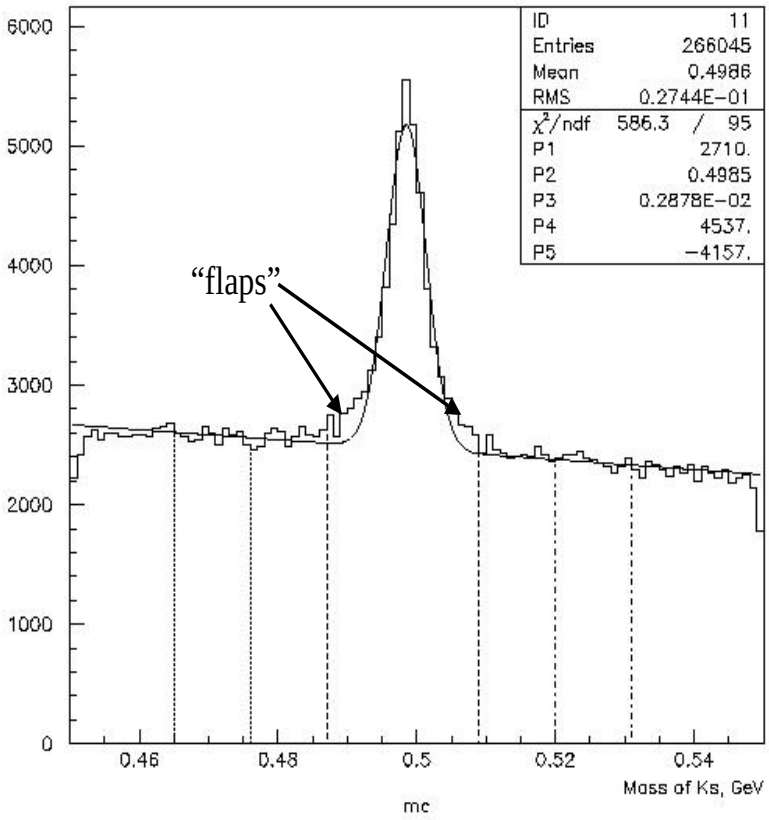


Figure 3.4: *Monte Carlo Candidates selected by the analysis. Single Gaussian fit.*

candidates can sometimes lie far enough from the mass peak so that the reconstructed candidate is mistaken for a background. This happens sometimes in the case of $K_S^0$ mesons: because the analysis selects $K_S^0$ candidates inclusively, their tracking parameters, e.g. momenta, may vary from one candidate to another. As a result the histogram on the mass plot is a sum of a large number of Gaussians with slightly different parameters and therefore it

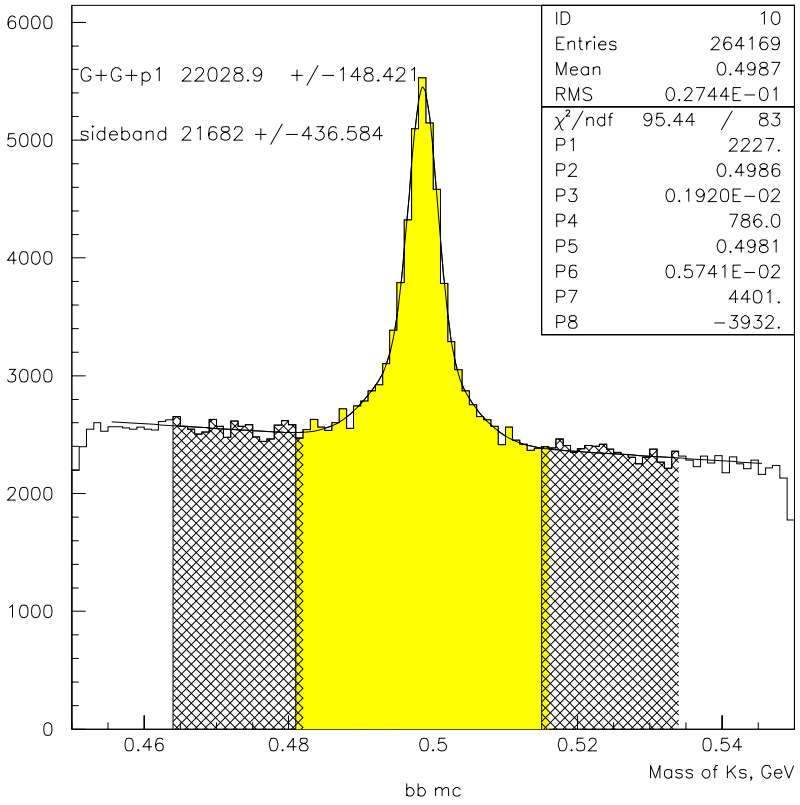


Figure 3.5: *Monte Carlo Candidates selected by the analysis. Double Gaussian fit. Also shown are sidebands and peak area.*

can not be very well described just by single Gaussian fit. However a double Gaussian usually fits the distribution fairly well. It consists of a narrow core Gaussian and a wider one for the tails, or "flaps," of the distribution. Both of the methods are studied in this document. Figure 3.5 shows the result of a double Gaussian fit on the same Monte Carlo distribution as in figure 3.4.

In addition to Gaussian fits, another method of counting the candidates

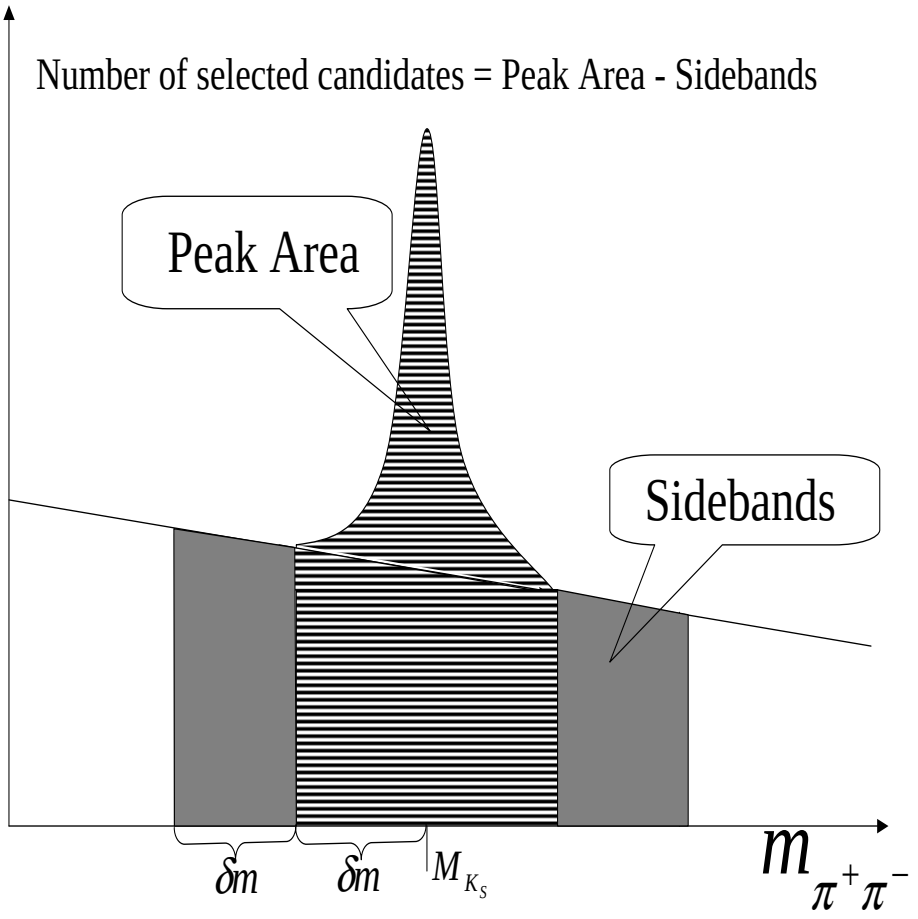


Figure 3.6: *Sideband Subtraction method illustrated schematically.*

is sideband subtraction, shown schematically in Figure 3.6. The number of particle candidates is obtained by subtracting the area of the "Sidebands" from the "Peak area." The "Peak area" is centered on the value of $M_{K_S^0}$ with a width of $2 \times \delta m$, where $\delta m$ is three times the $\sigma$ of the wider Gaussian from the double Gaussian fit. The $\delta m$ is also defined as the width of the "sidebands" and the "sidebands" are also equidistant from the central mass value $M_{K_S^0}$ and, in this particular case, are immediately adjacent to the "Peak

area." Generally, sidebands can be at some distance from the peak area. It is important to note that the particular choice of $\delta m$ does not change the overall $K^0_S$ count within the errors. For very small $\delta m < 2\sigma$ some of the signal can erroneously get assigned to a sideband region and for very large $\delta m > 5\sigma$ the assumption about the linearity of the background becomes invalid. In this analysis $\delta$ was varied in the region $\sigma < m < 5\sigma$ and the optimal value of $3\sigma$ was chosen to minimize both of the systematic effects mentioned above. Figure 3.4 shows the same Monte Carlo histogram as Figure 3.6 with the results of single Gaussian methods of $K^0_S$ counting and sideband subtraction. In this case, sidebands are $\delta m$ away from the peak area. It should be noted that the shape of the background in this method is assumed to be linear. In the case of $K^0_S$ this is true with the good precision and it is shown in Figure 3.8: the systematic error due to the non-linearity of the background is much smaller than the other dominating errors.

Figures 3.7 and 3.8 show various fits for $K^0_S$ peaks. From Figure 3.7 it is seen that a double Gaussian fit (two bottom plots) describes the $K^0_S$ peak much better than a single Gaussian fit (two top plots). Plots on the left side have been fitted with the first order polynomial (straight line) and on the right side with the second order polynomial (parabola). The background is well estimated either by first order polynomial (lower left plot) or by second order polynomial (lower right plot). In fact, the difference between the numbers of background tracks, as estimated with first and second order polynomial, is less than the standard deviation on the number of background tracks.

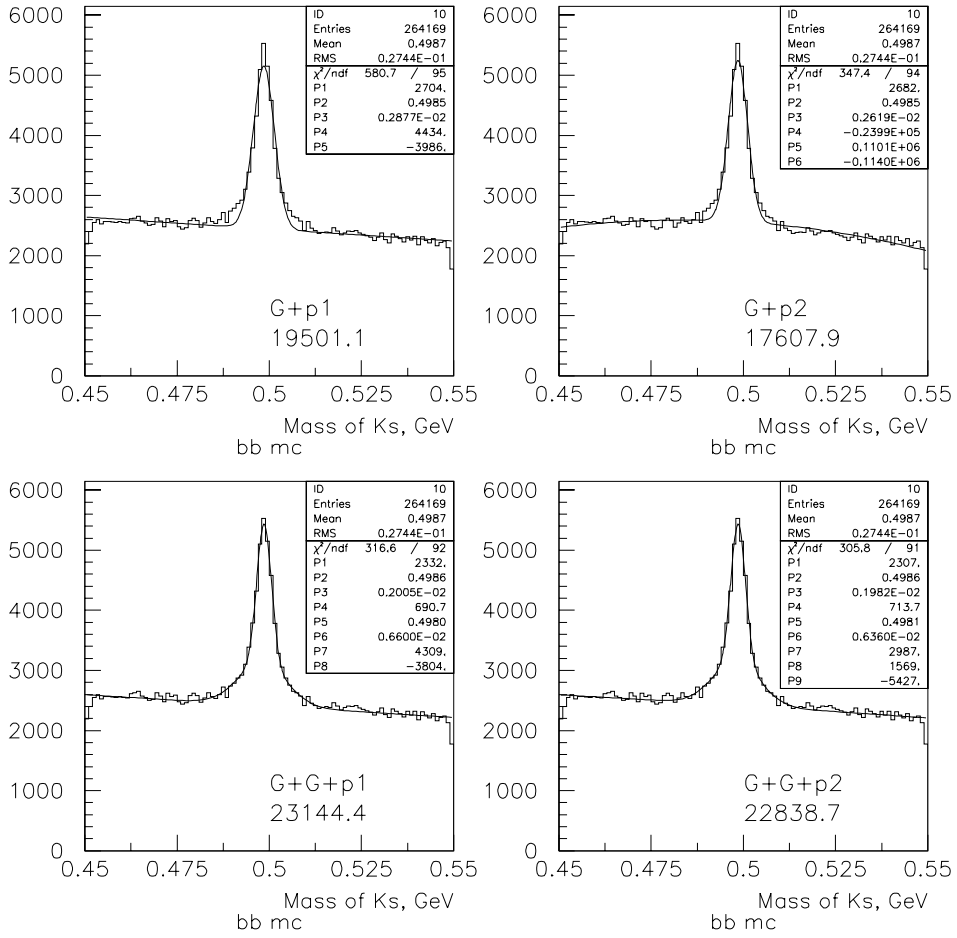


Figure 3.7: *Different fits using the generic $b\bar{b}$ Monte Carlo sample: Gaussian and first order polynomial, Gaussian and second order polynomial, double Gaussian and first order polynomial, double Gaussian and second order polynomial. The numbers of $K_S^0$ obtained by integrating the fits are shown on each fit. The double Gaussian fit describes the $K_S^0$ distribution significantly better than a single Gaussian fit.*

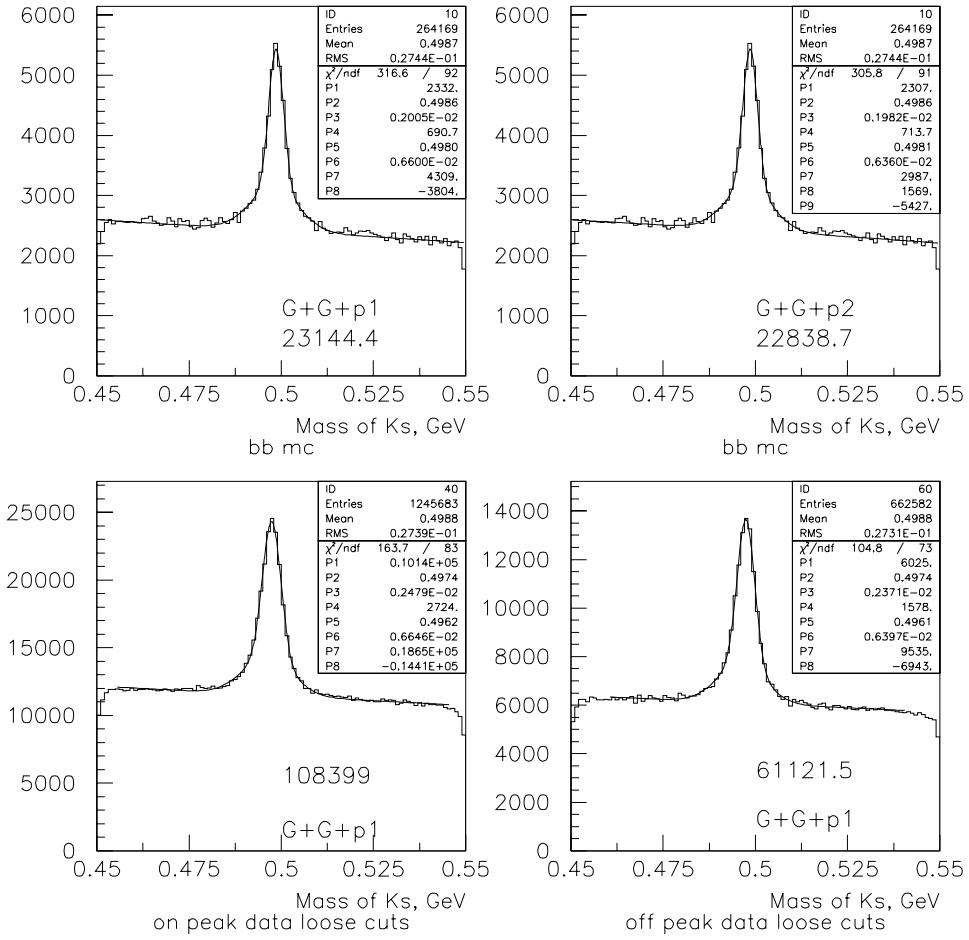


Figure 3.8: *Two fits for the generic $b\bar{b}$ Monte Carlo sample and on peak and off peak data samples. Note that, as can be seen from the first two plots, within the statistical error fitting the background with first order polynomial versus second order polynomial does not change the $K_S^0$ count.*

| Method of counting | Number of $K_S^0$ | Efficiency |
|---|---|---|
| Single Gaussian Fit | 19501±487 | $40.94 \pm 1.02\%$ |
| Double Gaussian Fit | 22029±148 | $46.25 \pm 0.31\%$ |
| Sideband Subtraction | 21682±437 | $45.52 \pm 0.92\%$ |

Table 3.3: *Efficiency of the selection as obtained from Monte Carlo.*

The lower plots of Figure 3.8 are double Gaussian plus first order polynomial fits for on peak and off peak data samples. Again, as it has been seen in Monte Carlo, a double Gaussian nicely fits the $K_S^0$ peaks in data samples too.

In Table 3.3 the corresponding reconstruction efficiency is calculated for Gaussian fits and sideband subtraction. Double Gaussian Fit result is in good agreement with sideband subtraction method.

## 3.4 Selection of candidates

The events selected for this inclusive analysis were recorded by the detector without any offline selection criteria applied to them. A minimal number of cuts that are generally considered to be loose, i.e. with the efficiencies close to 100%, has been applied to the collections of such events. The selection cuts are described in detail in the next chapter.

Any two oppositely charged tracks from the chosen selections of events were fed to a vertexing algorithm. This algorithm, called LeastChiVertexer,

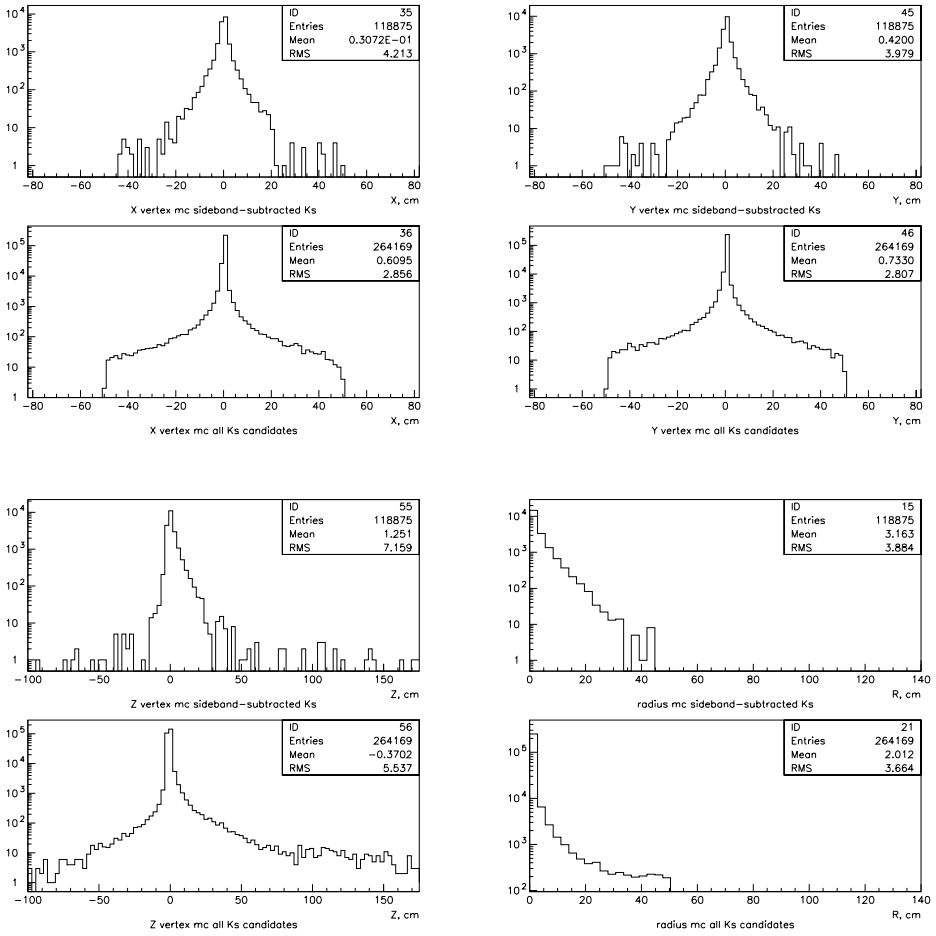


Figure 3.9: *Generic $b\bar{b}$ Monte Carlo Candidates selected by the analysis. Shown are four plots for the X, Y and Z coordinates and azimuthal radius of the vertex obtained by LeastChiVertexer. Top portions of each of the four plots contain $K_S^0$ candidates, bottom - all candidates in the mass window 0.45 to 0.55 GeV.*

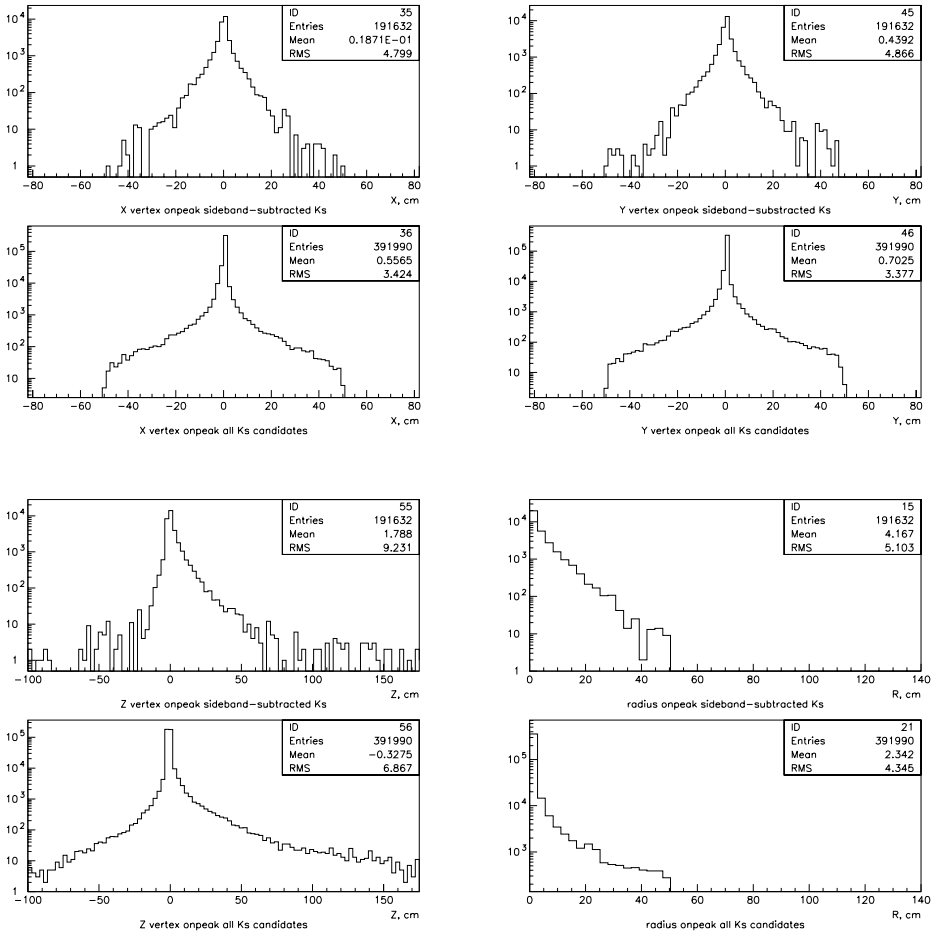


Figure 3.10: *Candidates selected by the analysis from the on peak data sample. Shown are four plots for the X, Y and Z coordinates and azimuthal radius of the vertex obtained by LeastChiVertexer. Top portions of each of the four plots contain $K_S^0$ candidates, bottom - all candidates in the mass window 0.45 to 0.55 GeV.*

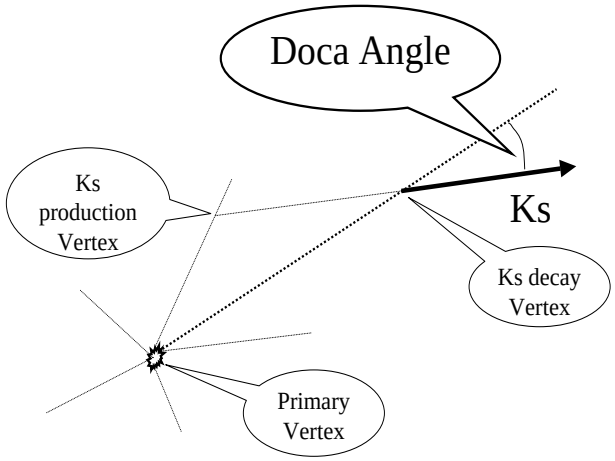


Figure 3.11: *Doca Angle shown schematically.*

combined two tracks and looked for their vertex. Only if the vertex was found the two daughter particles were assumed to have pion masses and their momenta were combined to produce the mass of their mother, i.e. $K_S^0$ candidate. $K_S^0$ candidates were selected in a 0.45 to 0.55 GeV mass window. Figure 3.9 shows the $K_S^0$ candidate vertex position obtained by the vertexing algorithm in generic $b\overline{b}$ Monte Carlo. Figure 3.10 shows the corresponding plots for on-peak data runs. Sharp steps at r=50 cm of the distributions on Figures 3.9 and 3.10 are due to the perpendicular radius[4] cut, $r < 50\,cm$.

Figure 3.12 presents the distributions of polar and azimuthal angles of $K_S^0$ candidates from Monte Carlo simulation in the XYZ frame. As can be seen from the bottom plots, the azimuthal angle distributions have a slight dip at around $0^0$. This slight asymmetry of the X-Y distributions can be explained by the non-collinearity of the beam and Z axes, and has no effect

[4]The radius is $r = \sqrt{x^2 + y^2}$

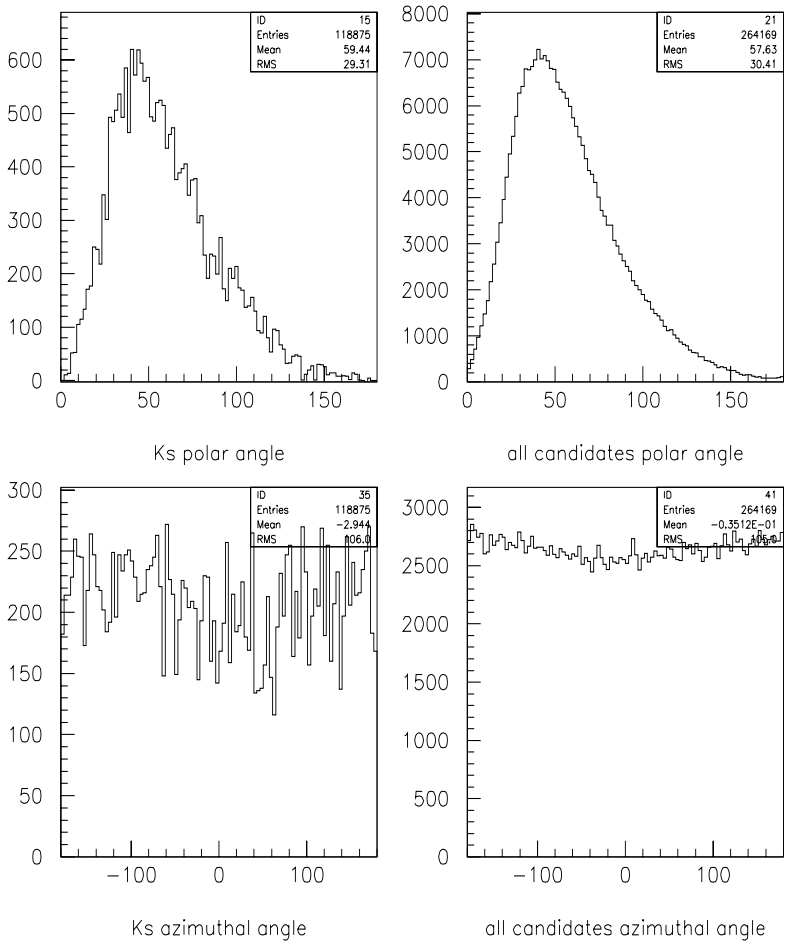


Figure 3.12: *Generic bb Monte Carlo data. Polar(top) and azimuthal(bottom) angles for Ks candidates in the Gaussian peak region(right) and all candidates (left) in the 0.45-0.55 mass window. The angles are defined by the momentum of the candidate in lab frame (i.e. with respect to Z axis instead of beam line).*

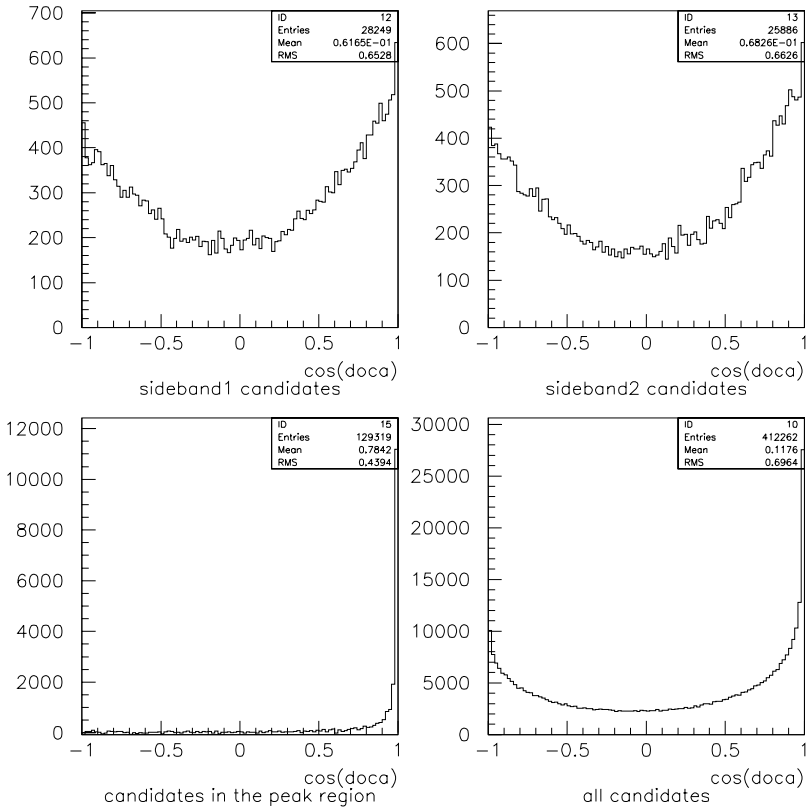


Figure 3.13: *Doca angle - the cosine of the angle between the momentum of the candidate and the direction to the primary vertex. Generic $b\overline{b}$ Monte Carlo plots for doca angles of the $K_S^0$ candidates in the sidebands and Gaussian peak region and all $K_S^0$ candidates.*

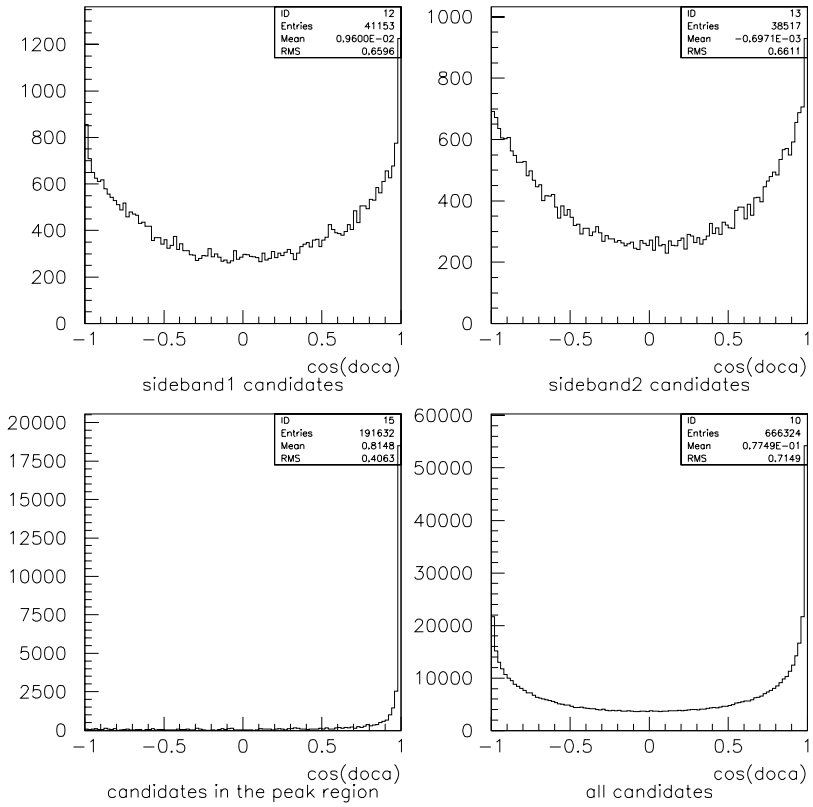


Figure 3.14: *Doca angle - the cosine of the angle between the momentum of the candidate and the direction to the primary vertex. On peak data plots for doca angles of the $K_S^0$ candidates in the sidebands and Gaussian peak region and all $K_S^0$ candidates.*

on the results.

Figures 3.13 and 3.14 show distance of closest approach (doca) angle distributions for generic $b\bar{b}$ Monte Carlo and on peak data samples. the $K_S^0$ candidates tend to have doca angle close or equal to $0^0$ (bottom left plots), while backgrounds have evenly distributed doca angles (top plots).

## 3.5 $K_S^0$ Candidate Selection Cuts

$K_S^0$ candidates were selected using five criteria, or cuts, listed below. Cuts 1 through 4 are standard for all analyses presented in this document. Cut 5 is generally stricter than cuts 1 through 4 and it rejects a lot of badly reconstructed candidates. It was used only for certain parts of the analysis where uniformly good quality of tracks was required. For the main branching fraction calculation cut 5 was not used. The selection of the values of cuts was made to reduce the systematic uncertainties while minimizing the statistical errors. The overall result does not depend significantly, i.e. is within the errors, with a $\sim 10\%$ variation of the values of cuts around the chosen values; proving that the choices of the cuts are stable.

$K_S^0$ candidates must posses the following criteria (further each of the cuts is explained in detail):

1. There is a secondary vertex in the event with two oppositely charged tracks and $\chi^2$ of the vertex fit is less than 20.

2. The invariant mass of the two tracks is 0.45-0.55 GeV.

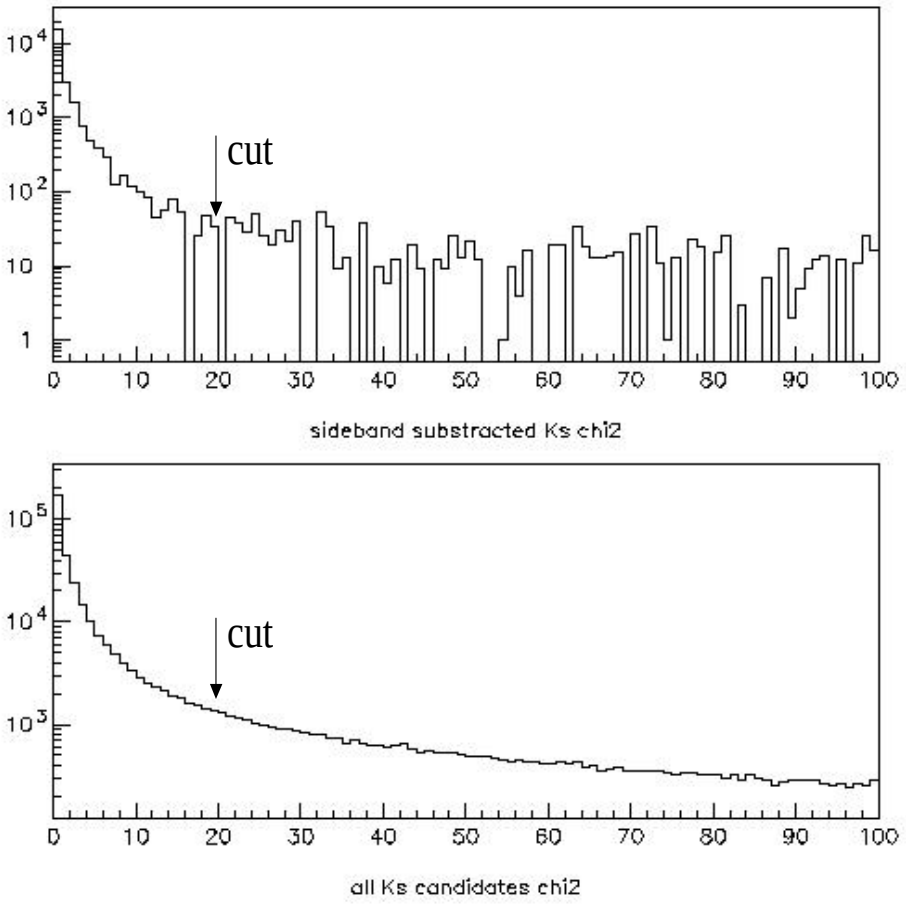


Figure 3.15: $\chi^2$ *of the* $K_s^0$ *candidates. Cut is chosen to be at* $\chi^2 < 20$.

3. Radius 0-50 cm.

4. Helicity cut $|cos\theta| < 0.9$.

5. Number of Drift Chamber Hits $> 20$.

Figure 3.15 shows the $\chi^2$ distribution of $K_s^0$ candidates. $\chi^2$ is a parameter computed by the vertexing algorithm for each candidate vertex, and it is

equal to the sum of the squares of the closest approach distances from the hits to the chosen trajectories. The smaller is the $\chi^2$ the better is the fit. The upper histogram shows only those $K_S^0$ candidates to which sideband subtraction procedure has been applied (see Figure 3.6) and therefore it illustrates the efficiency of the cut. The bottom histogram is a $\chi^2$ distribution of all $K_S^0$ candidates falling in the mass window between 0.45 and 0.55 GeV and it illustrates the amount of background removed by the cut.

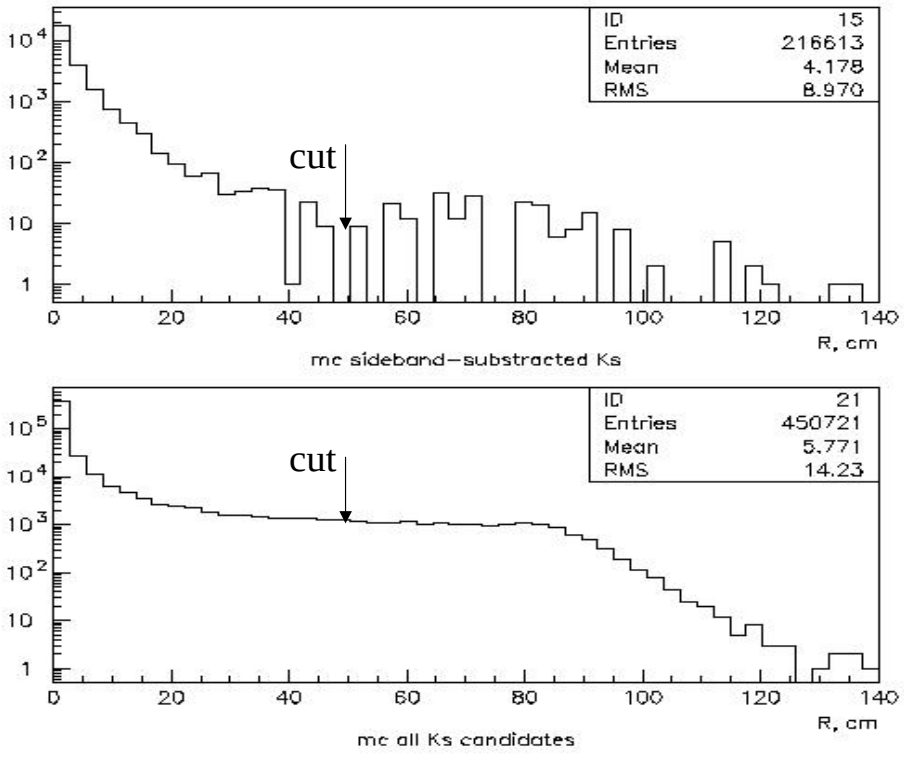


Figure 3.16: *Radius of the $K_S^0$ candidates.*

The radial distribution of $K_S^0$ candidates is shown in Figure 3.16. As in Figure 3.15, upper plot contains the radial distribution of the sideband

subtracted $K_S^0$ candidates and the lower plot shows the radial distribution of all $K_S^0$ candidates. The radius cut is chosen to be at 50 cm.

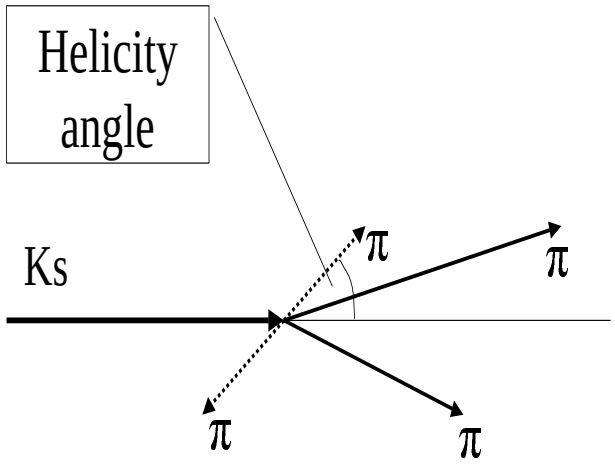


Figure 3.17: *Helicity Angle shown schematically.*

The helicity angle is defined as the angle between the $K_S^0$ momentum and the momentum of one of its daughter pions boosted into the $K_S^0$ rest frame. It is schematically shown on Figure 3.17. Figure 3.18 shows the absolute value of the cosine of the helicity angle of the $K_S^0$ candidate. Again, on the top histogram shown are sideband subtracted candidates and on the bottom - all candidates. For the analysis only those $K_S^0$ the candidates with absolute values of the cosine of helicity angle of less than 0.9 were accepted: $|cos\theta| < 0.9$.

The helicity cut efficiently removes candidates for which one of the daughters has been wrongfully assigned to be a pion. For example, the following decay $\Lambda \rightarrow p\pi^-$ can sometimes be misidentified as $K_S^0 \rightarrow \pi^+\pi^-$ and it is efficiently selected by helicity cut because if $p$ is misidentified as $\pi^+$ its helicity

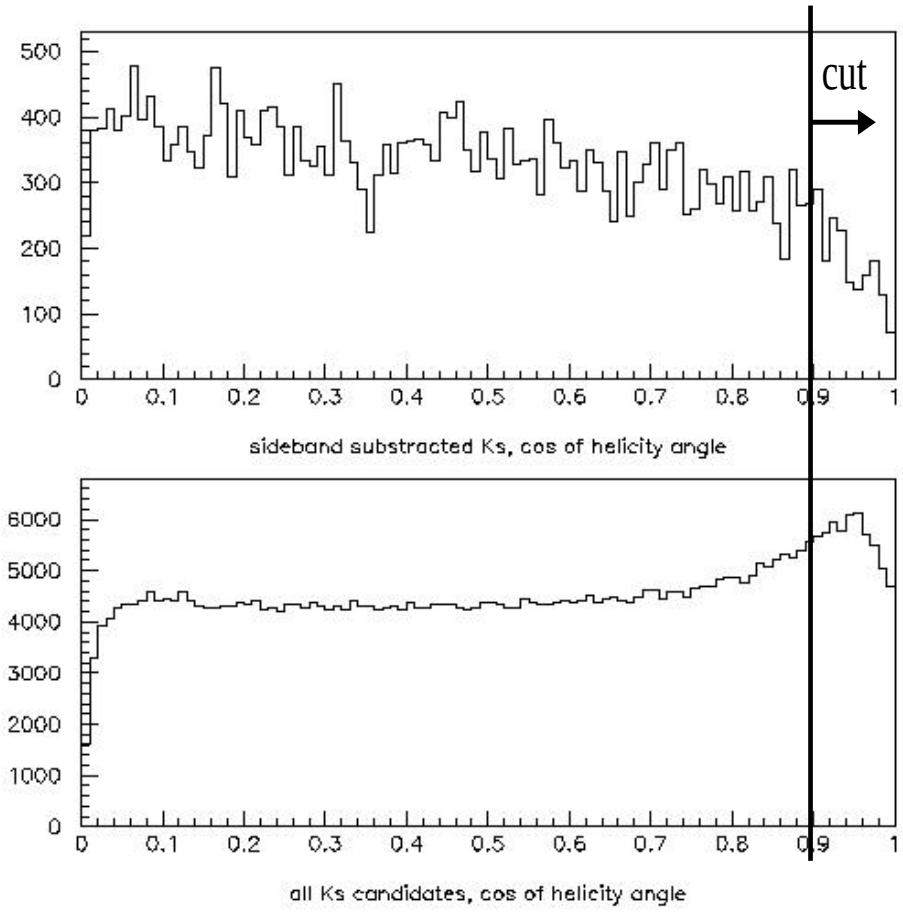


Figure 3.18: *Helicity of $K_S^0$ candidates.*

tends to be close to one. Figure 3.19 is a plot of mass of the candidate versus $|cos\theta|$, i.e. the distribution on the bottom of Figure 3.18 plotted versus mass of the candidate. The darker region to the right of the $|cos\theta| = 0.9$ line is background removed by the cut.

Figure 3.20 shows the number of hits that pions from $K_S^0 \to \pi^+\pi^-$ leave in the Drift Chamber. The cut of $N_{DCH\,hits} > 20$ is used to improve the

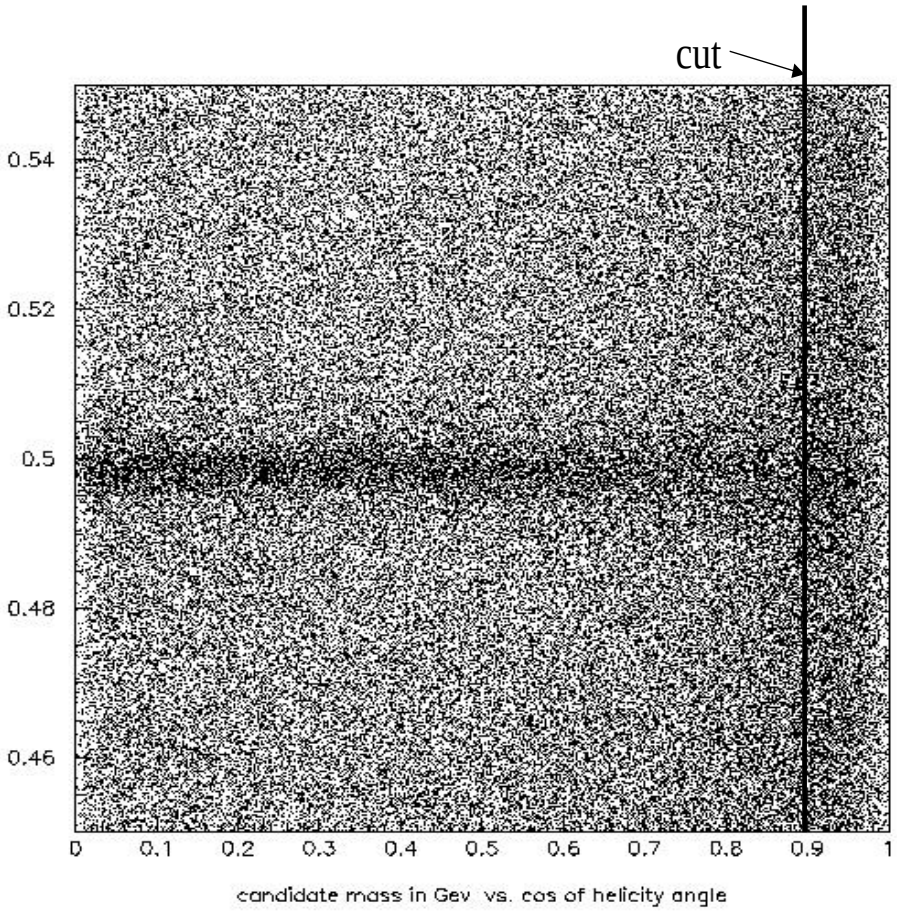


Figure 3.19: *Plot of the Mass of the $K_S^0$ candidates vs. the helicity.*

quality of the selected tracks.

Using loose cuts for selection of $K_S^0$ candidates results in $K_S^0$ mass plots having a wide variety of candidates with different tracking parameters. This in turn widens the $K_S^0$ mass peak making it hard to fit with a single Gaussian as it was described in detail in section 3.3. Figure 3.4 (also shown in section 3.3) illustrates the fact that $K_S^0$ mass peak with loose cuts does not fit well

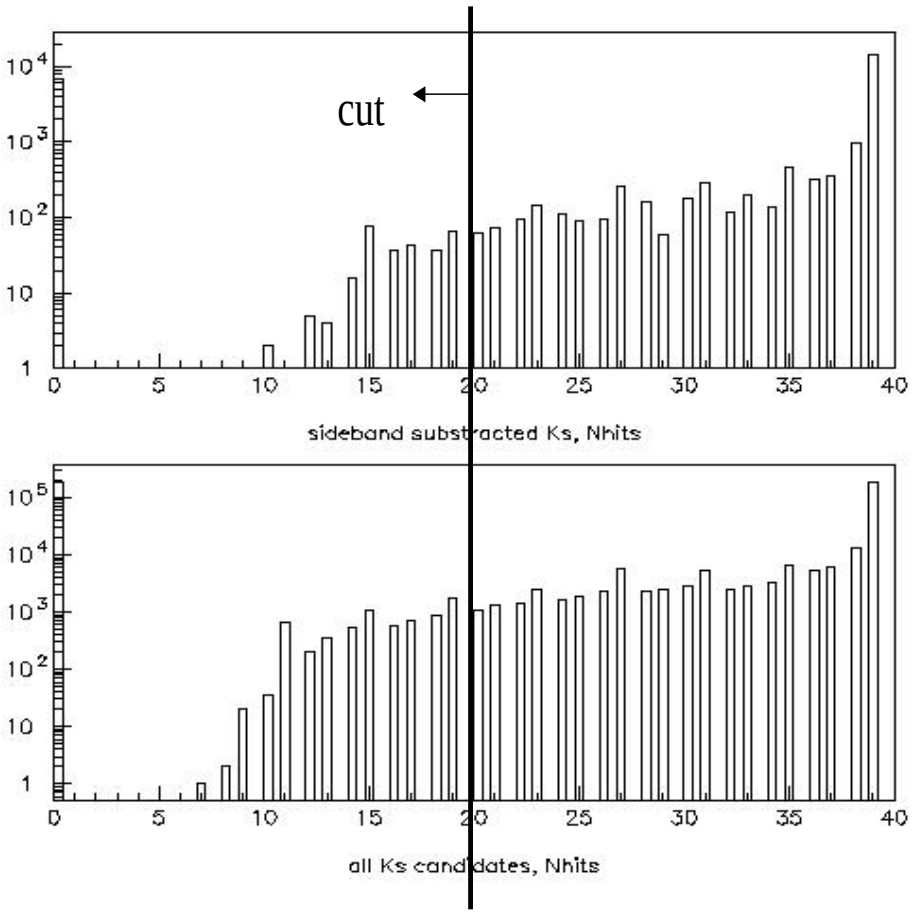


Figure 3.20: *Number of hits in the Drift Chamber.*

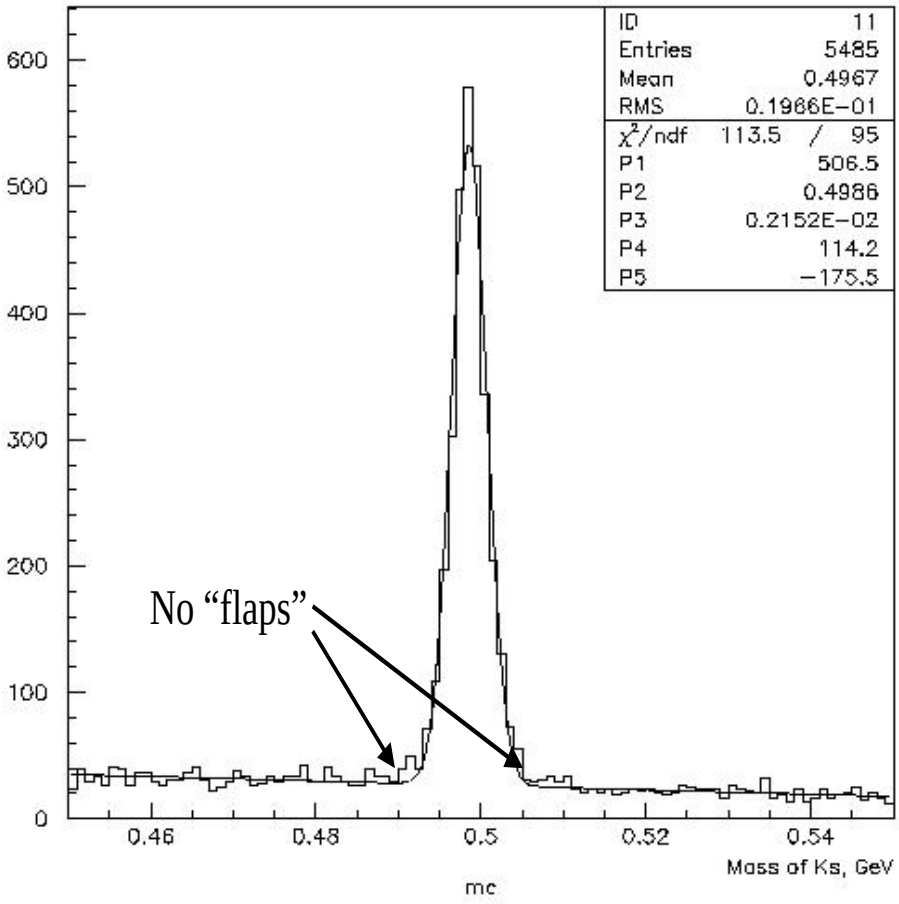


Figure 3.21: $K_s^0$ *mass distribution. Tight cuts (see cut 5).*

under a single Gaussian. So called "flaps" on the sides of the Gaussian are clearly notable. By tightening the selection criteria one can achieve better track quality and hence the better fit of the mass histogram. Figure 3.21 shows the same histogram as Figure 3.4 only with much tighter cuts. The "flaps" at the sides of the Gaussian are completely cut out, however, a large portion of the signal is also cut out. And at last, the top of Figure 3.22 is

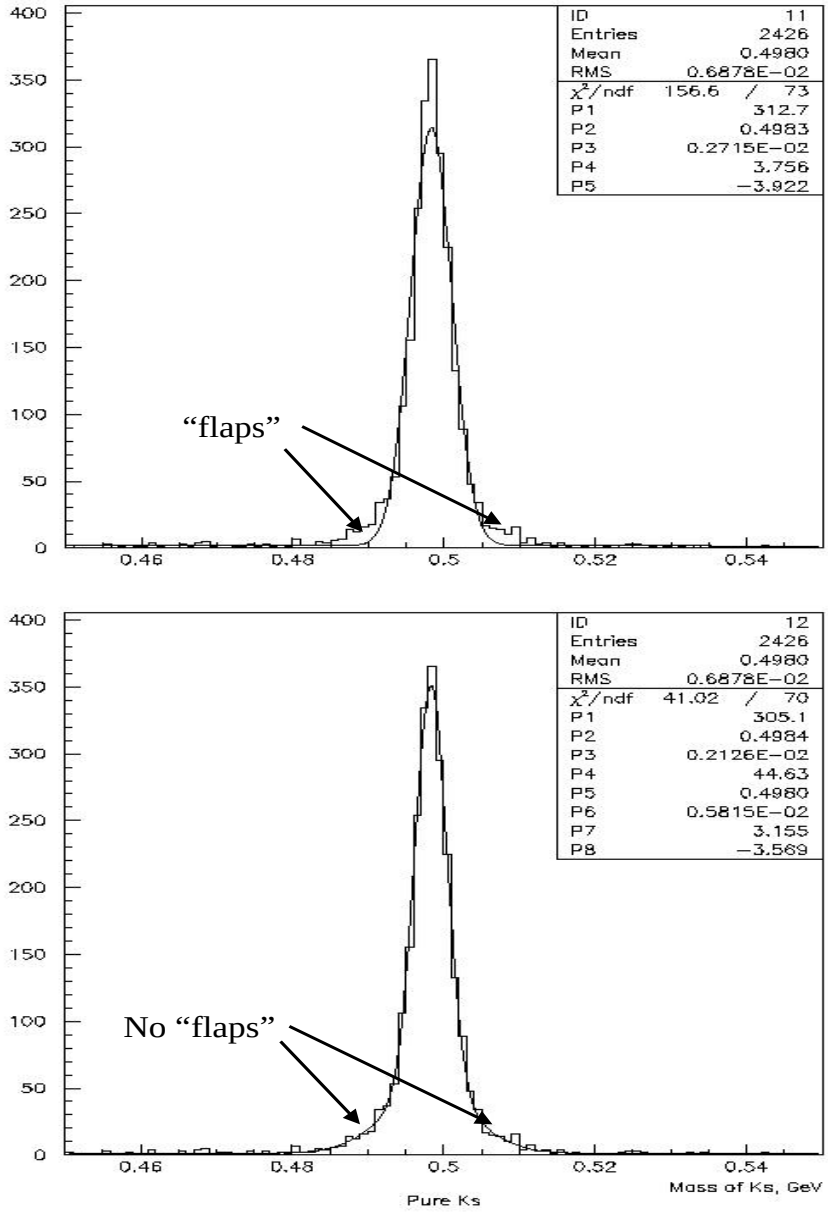


Figure 3.22: *$K^0_S$ mass distributions for Monte Carlo sample of pure $K^0_S$. Fitted with a single Gaussian (top) and a double Gaussian (bottom).*

a distribution of reconstructed $K_S^0$ candidates from a pure $K_S^0$ Monte Carlo sample fitted with a single Gaussian. It can be seen that the "flaps" are present in pure $K_S^0$ sample too. Therefore they are indeed caused just by badly reconstructed tracks rather than misidentified background particles. However these "flaps" can be well fitted with a double Gaussian fit. On the bottom of Figure 3.22 the same pure $K_S^0$ mass distribution is fitted with a double Gaussian. This time the fit covers the histogram quite nicely with no "flaps" left out[5].

## 3.6 Momentum and Mass Study

In addition to the main task of calculating the inclusive $K_S^0$ branching fraction several other studies have been carried out. For example, to better understand the reconstruction of $K_S^0$ some mass and momentum distributions of $K_S^0$ candidates have been analyzed. To study the dependence of reconstructed mass of the $K_S^0$ candidates on $K_S^0$ momentum all candidates have been grouped in 6 bins in momentum with 0.5 GeV/c steps. For each momentum interval mass histograms (see Figures 3.23 and 3.24) were plotted and then fitted with a single Gaussian. Plotted on Figure 3.25 are the fitted peak values of those Gaussians together with the errors of the fit. Solid crosses represent the $b\overline{b}$ Monte Carlo. Dashed crosses are on peak data points and straight line is Particle Data Group Value. The vertical axis corresponds

[5]Note that $\chi^2$ for double Gaussian fits is always smaller than for the single Gaussian fit of the same histogram. This also indicates a better fit.

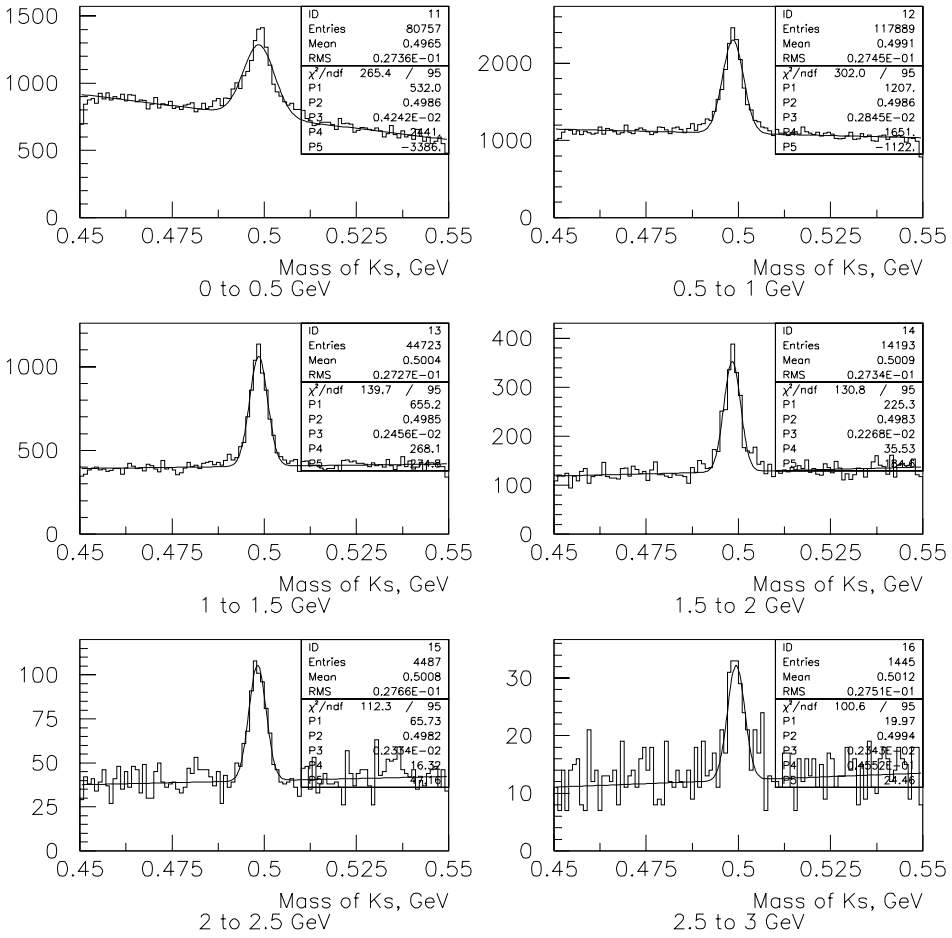


Figure 3.23: *Monte Carlo generic $b\bar{b}$. $K^0_s$ mass peaks for six 0.5* GeV/c *momentum bins, each fitted with a single Gaussian. The following set of cuts have been applied: radius<50cm, $|cos(helicity\ angle)|$ <0.9, vertex fitted with $\chi^2$ <20.*

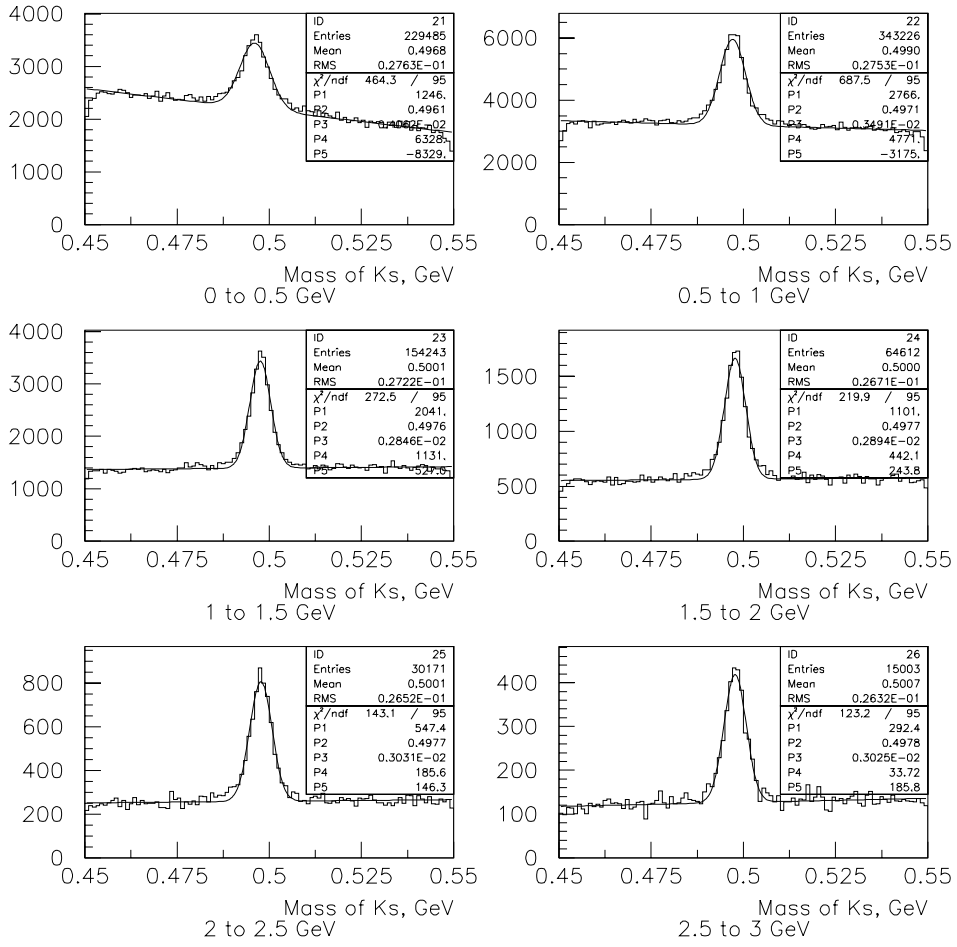


Figure 3.24: *On peak data. Ks mass peaks for six 0.5* GeV/c *momentum bins, each fitted with a single Gaussian. The same set of cuts have been applied: radius<50cm, |cos(helicity angle)| <0.9, vertex fitted with* $\chi^2$ *<20.*

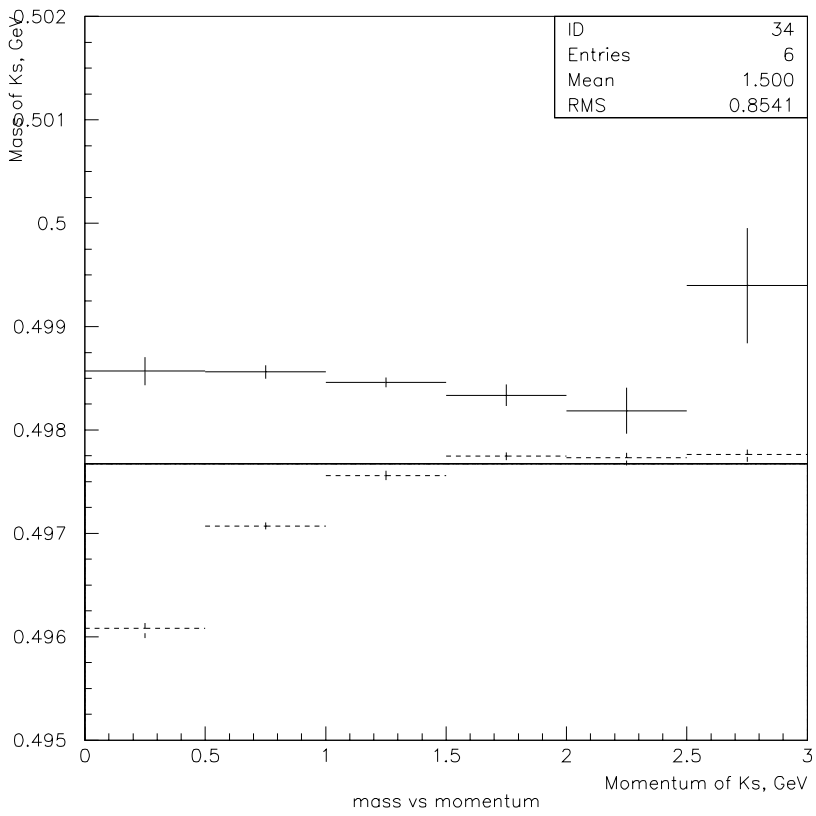


Figure 3.25: *Fitted mass values from Figure 3.23 and Figure 3.24 are plotted. Monte Carlo and Data are labeled with solid crosses and dashed crosses respectively. Errors shown are the errors on a Gaussian fit. s The straight line is a PDG value.*

to the mass values and horizontal to the momenta. Because the vertical scale is made to be rather fine (one quarter of MeV), several small effects can be noticed. One would be that the Monte Carlo predicts the $K_S^0$ mass to be

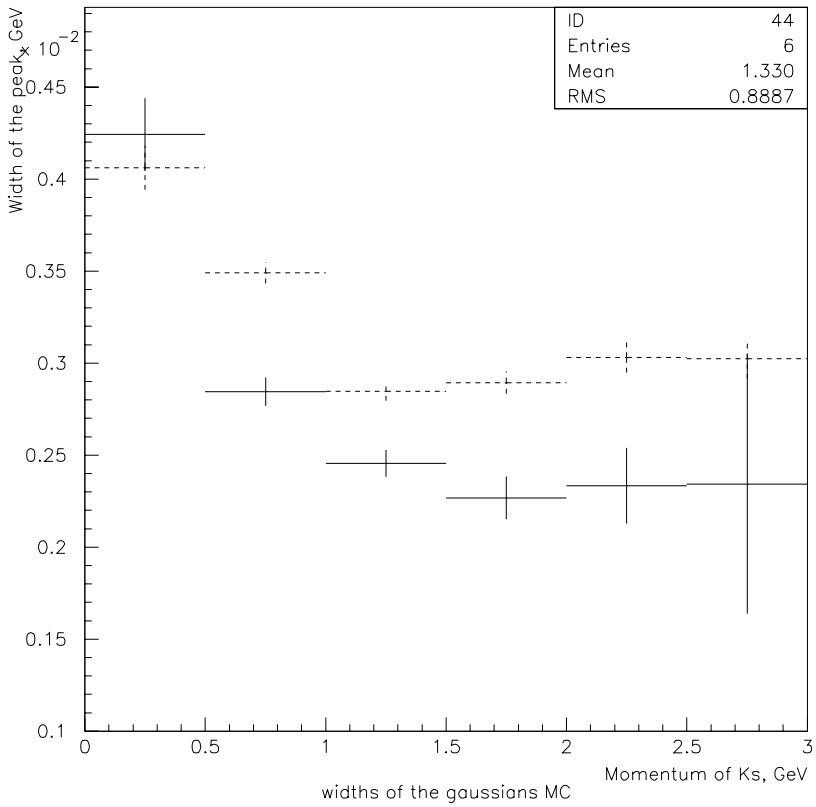


Figure 3.26: *Gaussian widths from are Figure 3.23 and Figure 3.24 plotted with solid and dashed crosses respectively. Errors shown are the errors on Gaussian fit.*

about 0.5 - 1 MeV higher than the world average. It has been a known effect observed in other analyses [31]. And although this higher mass effect has not been completely understood, its absence in the real data indicates that this is a problem in simulation rather than reconstruction. Another "feature" that

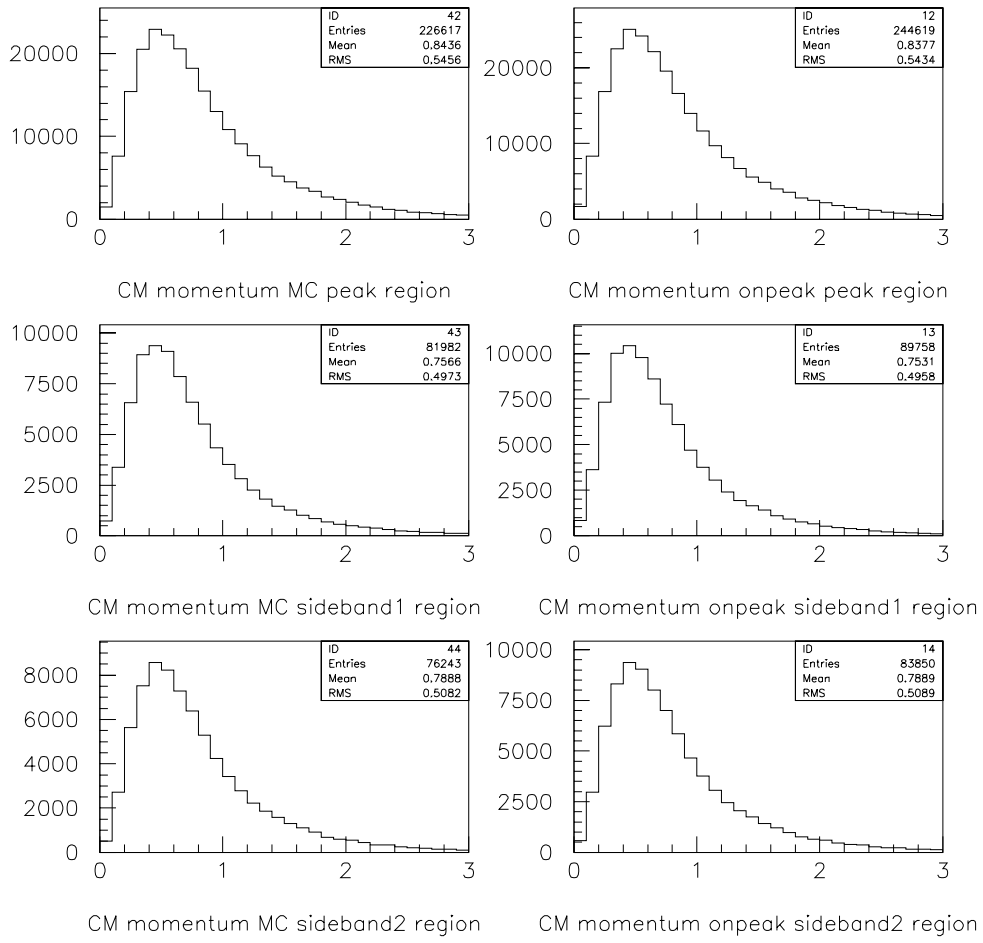


Figure 3.27: *Center of mass frame $K_S^0$ momentum (in* GeV/c *) distributions for generic $b\bar{b}$ Monte Carlo and on peak data samples. The candidates in the mass peak and from the sidebands of the mass peak are shown. One can see that the slower momentum candidates are more dominant in the background(sideband plots).*

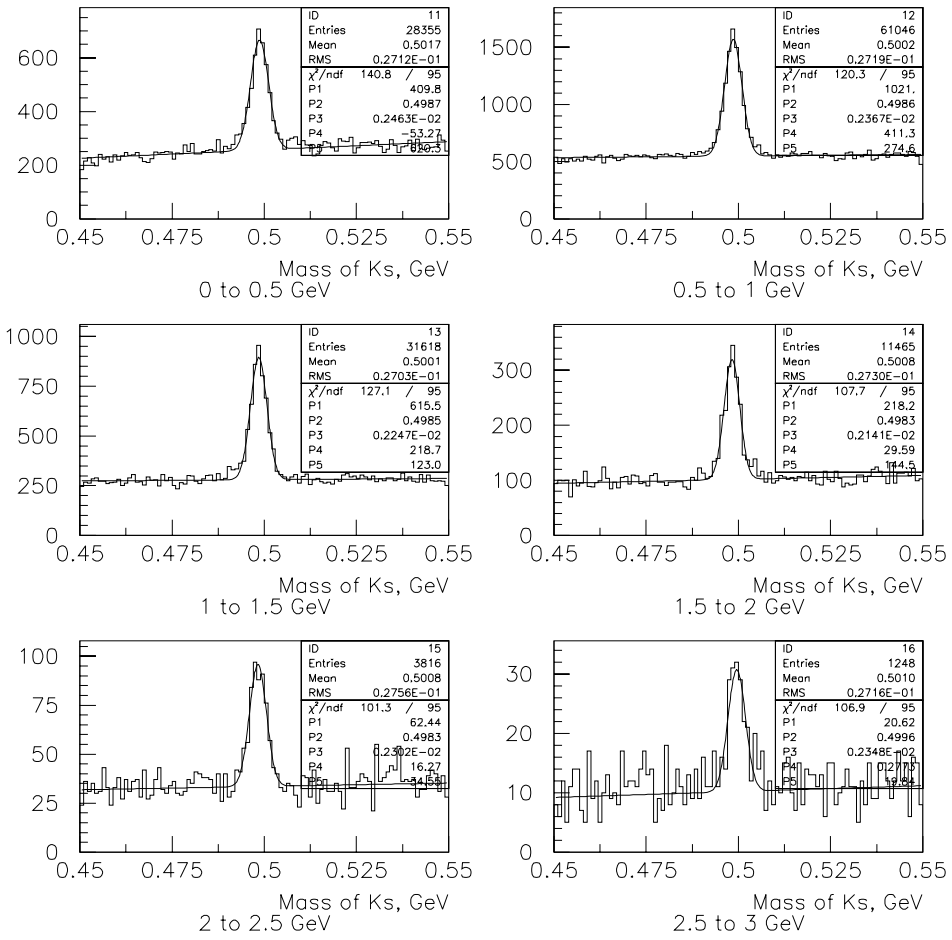


Figure 3.28: *Monte Carlo generic $b\bar{b}$. $K^0_S$ mass peaks for 6 momentum bins in 0.5* GeV/c *bins. Fitted with single Gaussian. The generic set of cuts have been applied: radius<50cm, $|cos(helicity\ angle)|$ <0.9, vertex fitted with $\chi^2$ <20. In addition Dchhits>20 cut has been applied.*

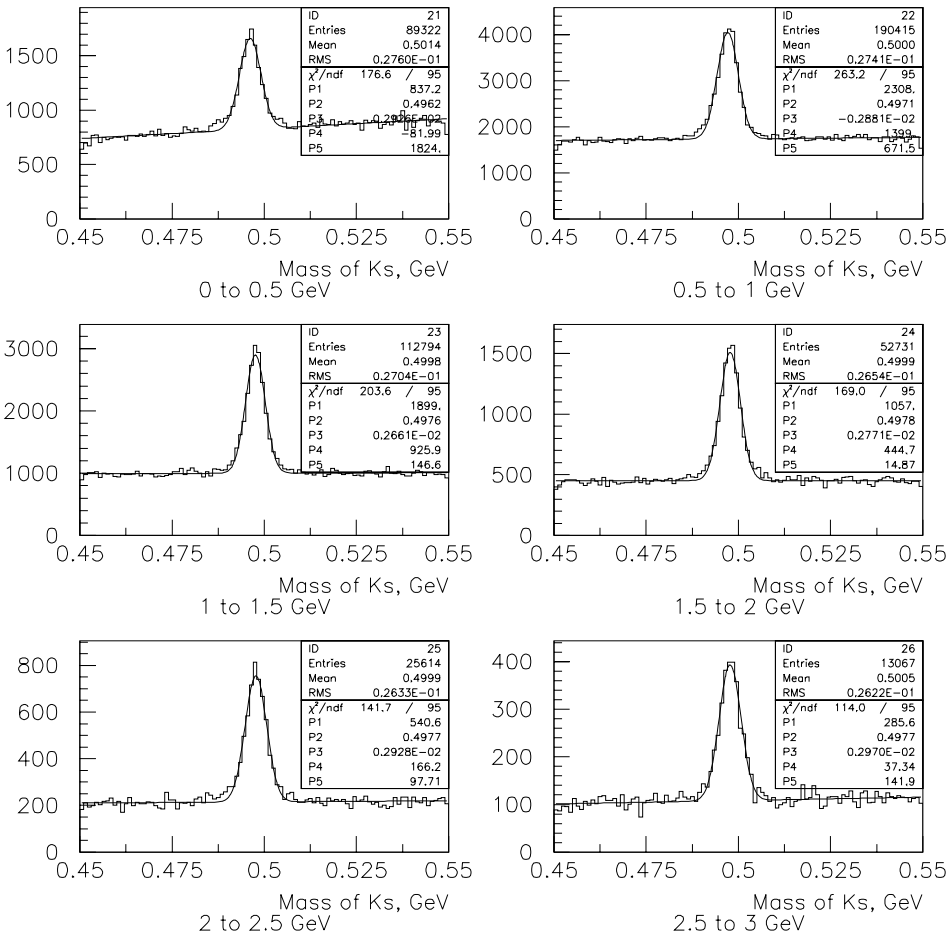


Figure 3.29: *On Peak data. Ks mass peaks for 6 momentum bins in 0.5* GeV/c *bins. Fitted with single Gaussian. The generic set of cuts have been applied: radius<50cm, |cos(helicity angle)| <0.9, vertex fitted with* $\chi^2$ *<20. In addition Dchhits>20 cut has been applied.*

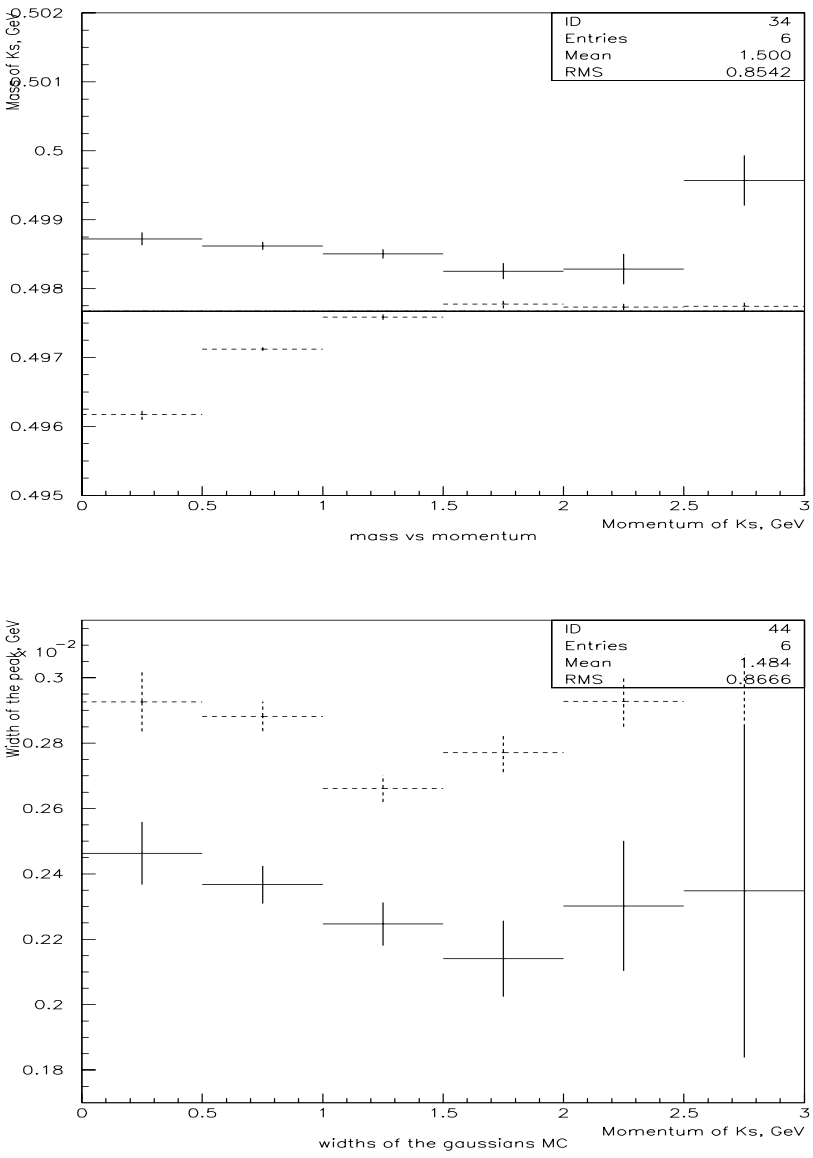


Figure 3.30: *Fitted mass values(top) and widths(bottom) from Figures 3.28 and 3.29 are plotted. Monte Carlo and data are labeled with solid crosses and dashed crosses respectively. Errors shown are the errors on Gaussian fit. The straight line is a PDG value.*

could clearly be seen on the Figure 3.25 is the drop of mass value for the real data in two low momentum bins. This has also been confirmed by other analyses [31], and although there has been no unequivocal explanation for this effect there are a few possible contributors. Inaccurate magnetic field mapping or mutual alignment between the Silicon Vertex Tracker and the Drift Chamber can be two possible reasons.

Figure 3.26 is a plot of the widths of the Gaussians from Figures 3.23 and 3.24 shown together with their errors. From this plot it can be seen that the $K_S^0$ peaks are getting narrower with the higher momentum. It is natural since slower momentum tracks tend to be harder to reconstruct and have higher backgrounds. Generally, the candidates from the sidebands tend to have lower momentum than those from the histogram peak area. (See Figure 3.27.)

Figures 3.28, 3.29 and 3.30 present the same procedure as in Figures 3.23 through 3.26 only this time track quality cut - number of Drift Chamber Hits $> 20$ - has been applied. The same general characteristics of masses and widths plots are seen in this case as well (see Figure 3.30). From this we can conclude that the tightening of the requirements on tracks does not change the overall agreement of the studied properties of the data and the Monte Carlo Simulation.

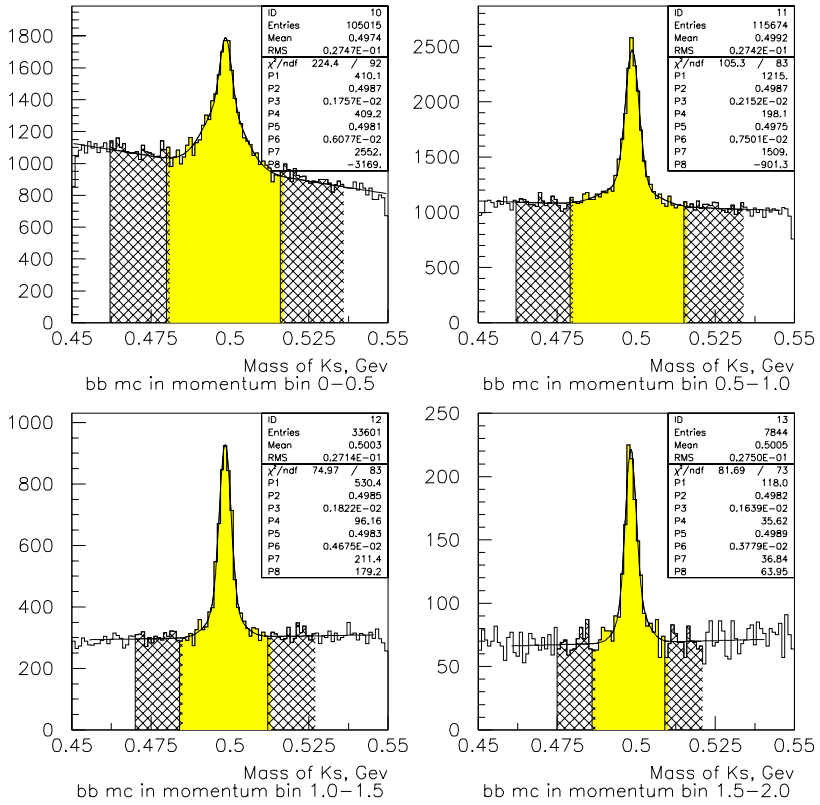


Figure 3.31: *Double Gaussian and first order polynomial fits for the generic $b\bar{b}$ Monte Carlo sample are shown. The candidates are grouped in 4 center of mass frame momentum bins. The widths of the second Gaussians for low momentum $K_S^0$ are larger than those for high momentum $K_S^0$.*

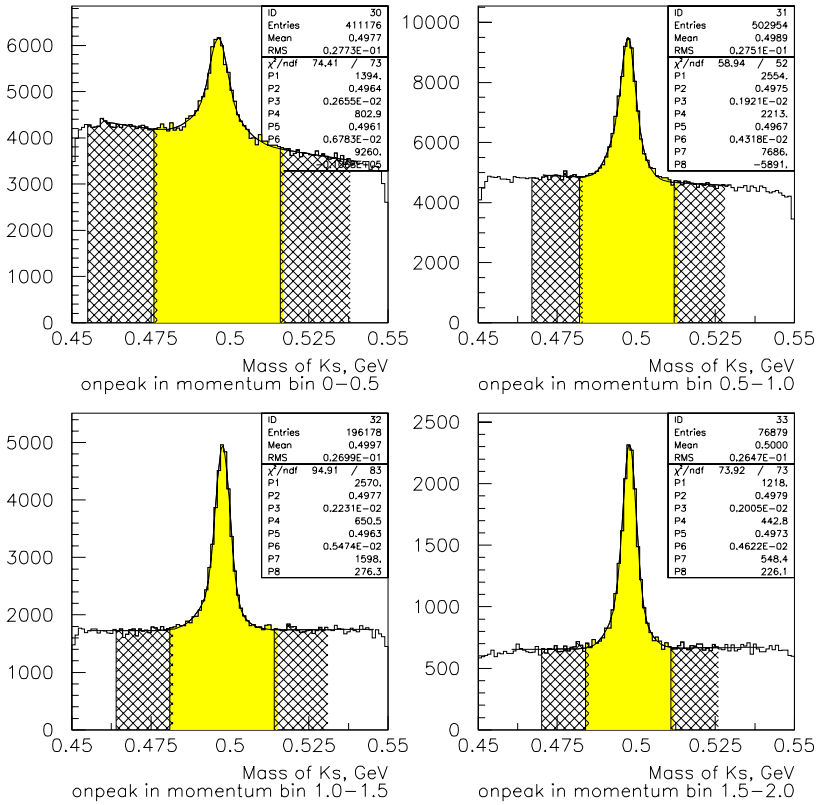


Figure 3.32: *Double Gaussian and first order polynomial fits for the on peak data sample are shown. The candidates are grouped in 4 center of mass frame momentum bins. The widths of the second Gaussians for low momentum $K_S^0$ are larger than those for high momentum $K_S^0$.*

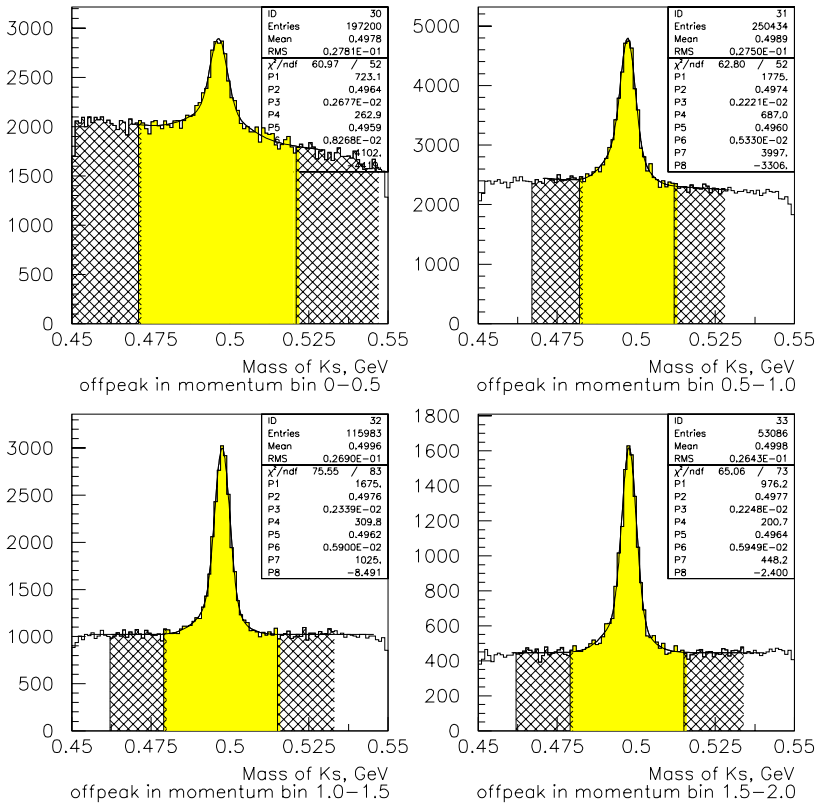


Figure 3.33: *Double Gaussian and first order polynomial fits for the off peak data sample are shown. The candidates are grouped in 4 center of mass frame momentum bins. The widths of the second Gaussians for low momentum Ks are larger than those for high momentum Ks.*

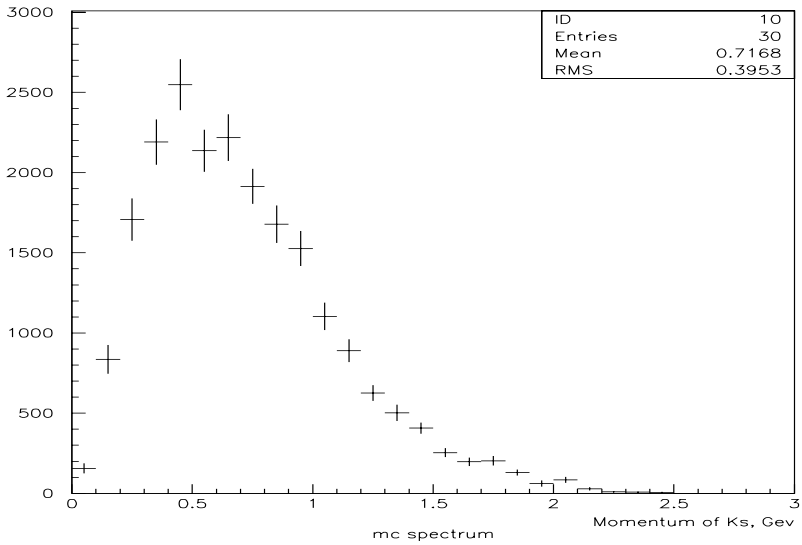


Figure 3.34: *Generic $b\bar{b}$ Monte Carlo. Reconstructed $K_S^0$ spectrum.*

## 3.7 Differential Multiplicities

Differential multiplicity is the fraction of $K_S^0$ mesons produced within a certain momentum range (0.1 GeV/c in this study) per B meson.

First, all $K_S^0$ candidates are grouped in 0.1 GeV center of mass (c.m.s) momentum[6] bins from 0 GeV/c to 3 GeV/c. Then the $K_S^0$ candidates in each bin are reconstructed and counted using the analysis routine (described in chapter 3.4). The method of counting for the differential multiplicity study was chosen to be the double Gaussian fit integration since it describes the $K_S^0$ distributions the best. Thus, for each data sample (on peak, off peak

[6]Everywhere in this chapter unless specified the momentum of the $K_S^0$ candidate is in the center of mass frame.

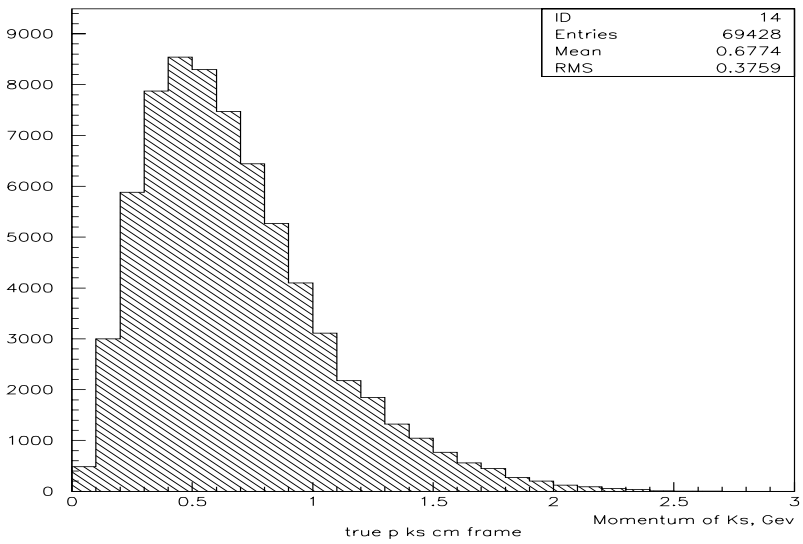


Figure 3.35: *Generic $b\bar{b}$ Monte Carlo. $K_S^0$ spectrum from truth table.*

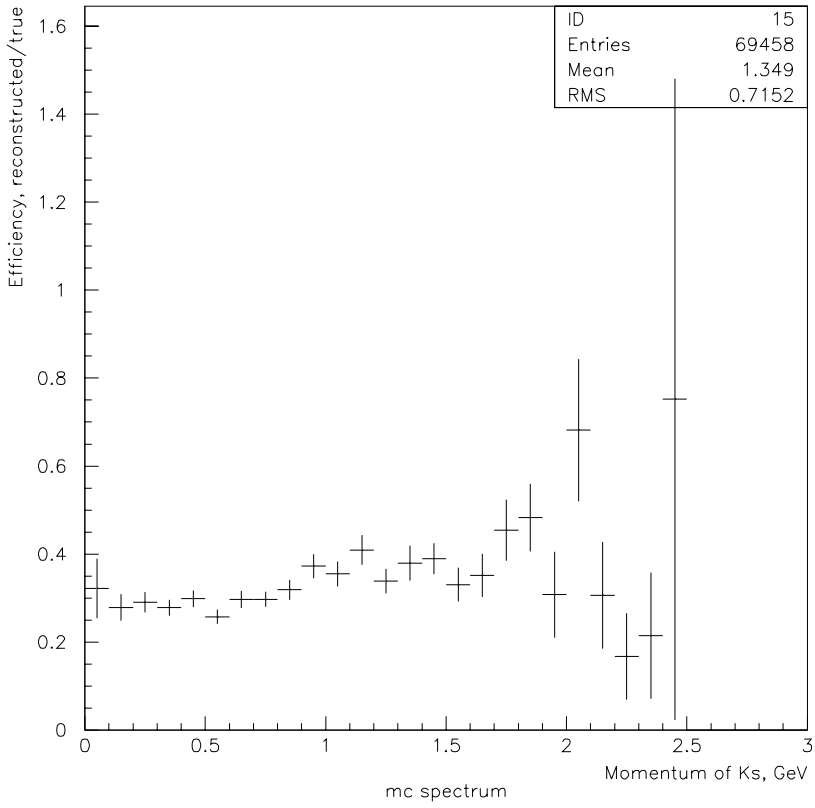


Figure 3.36: *The ratio of reconstructed mc $K_s^0$ spectrum over true $K_s^0$ spectrum. I.e. bin by bin reconstruction efficiency.*

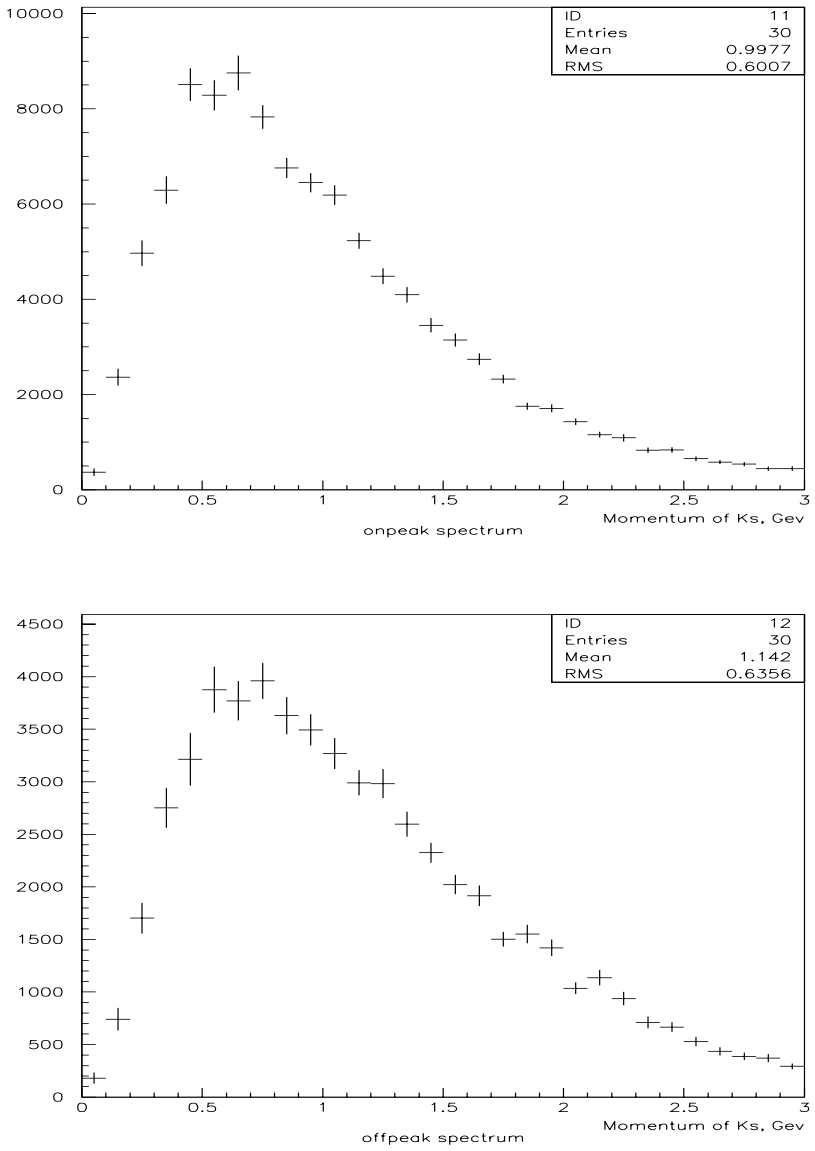


Figure 3.37: *$K_s^0$ spectrum observed in on peak (top) and off peak (bottom) data.*

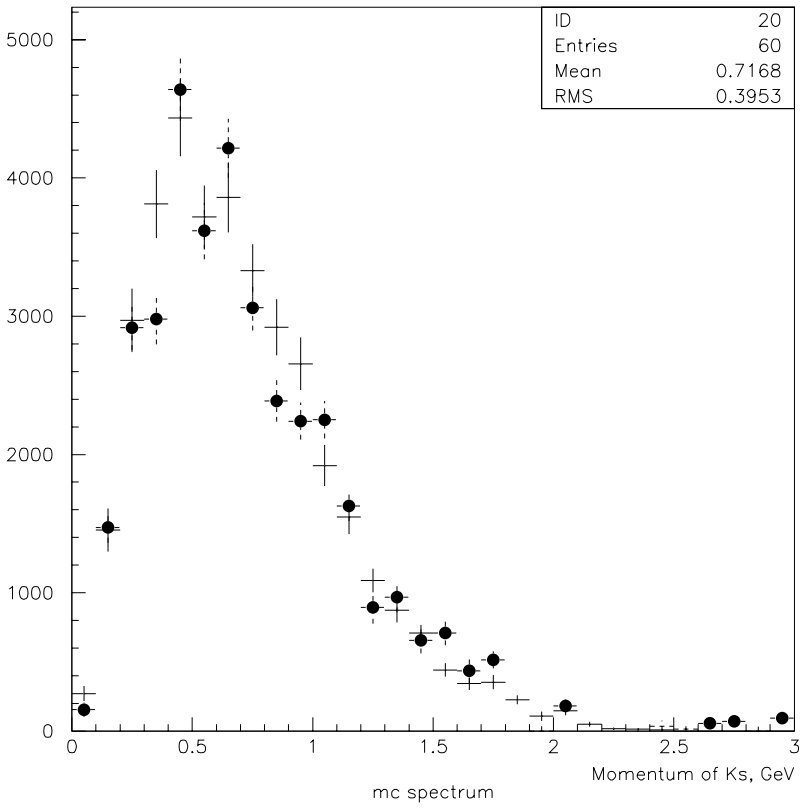


Figure 3.38: *Continuum subtracted $K_s^0$ spectrum(points) overlayed with generic $b\overline{b}$ Monte Carlo reconstructed $K_s^0$ spectrum.*

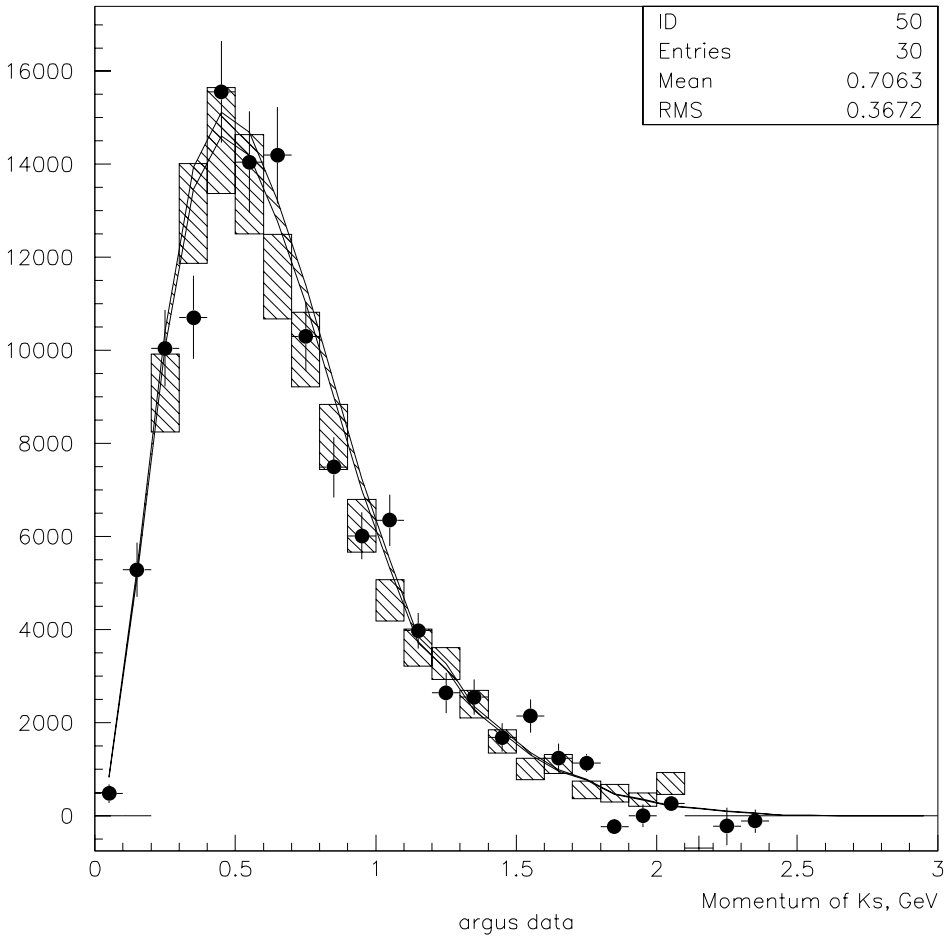


Figure 3.39: *Efficiency unfolded $K_s^0$ spectra. Obtained by dividing the spectra in Fig 3.38 by differential efficiencies from Fig 3.36. Solid points in Fig 3.38 correspond to solid points in this Fig(data points). Monte Carlo crosses in Fig 3.38 when divided by efficiencies return MC Truth spectrum(continuous curve). Overlayed with Argus' measurement(boxes). Statistical and systematic errors are added in quadratures and shown by the error bars.*

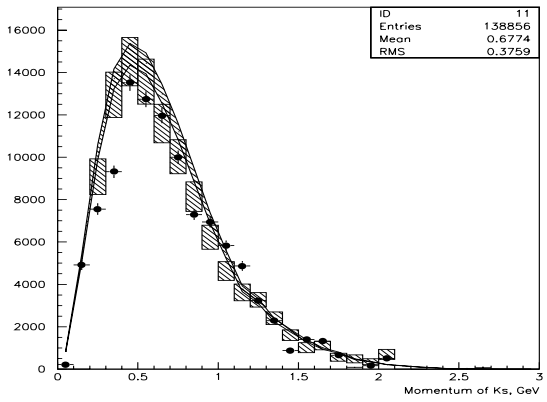


Figure 3.40: *Old efficiency unfolded $K_S^0$ spectra(same as Fig 3.39). The method used to obtain this plot didn't consider the relationship of sideband widths on momentum. Instead the fixed values of sidebands were used. This lead to some loss of slow $K_S^0$ due to the fact that sidebands become significantly wider in low momentum region.*

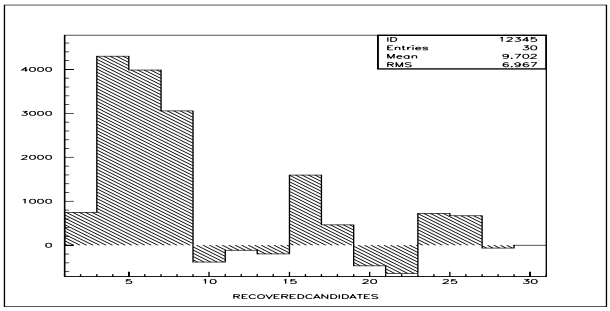


Figure 3.41: *Shown is the difference between the spectrum in Figure 3.39 and 3.40. The peak in the lower momentum region is due to the $K_S^0$ recovery in bin by bin counting. The momentum shown is in 0.1* GeV *units.*

and Monte Carlo) thirty double Gaussians have been fitted to count the $K_S^0$ in each momentum bin. Figures 3.31, 3.32 and 3.33 show the double Gaussian fits for the three samples: Monte Carlo data, on peak data and off peak data respectively. The momentum binning range in these figures is 0.5 GeV/c which is actually five times as coarse as the one used to obtain the multiplicities.

Another, simpler way of obtaining the $K_S^0$ count for different momentum bins is preselecting the $K_S^0$ candidates first using sideband subtraction applied to all range of momenta and then plotting the momentum distribution for the selected $K_S^0$s. This approach might be less accurate since the sideband width varies significantly with momentum and this should be taken into account. Indeed, for example, Figure 3.31 shows the $K_S^0$ candidates grouped in four momentum ranges 0-0.5, 0.5-1.0, 1.0-1.5 and 1.5-2.0. For each of the ranges the double Gaussian fits and sidebands are shown. It can be seen that for slower $K_S^0$ candidates the widths of the fits and sidebands are larger than the widths of the faster $K_S^0$s. In fact the width of the sidebands in the 0-0.5 GeV range is larger than the width of the sidebands for the overall $K_S^0$ distribution (like one in Figure 3.5). This results in the undercounting of slow $K_S^0$ and it is illustrated in Figures 3.40 and 3.41.

This undercounting was the reason why the $K_S^0$ have been analyzed carefully bin by bin. Figure 3.34 shows the summary of the counts (with statistical errors) of $K_S^0$ bin by bin in 30 bins. To obtain the efficiency of the analysis the histogram in Figure 3.34 needs to be divided bin by bin by the actual or "true" numbers of $K_S^0$ generated by the Monte Carlo. The information

about the "true" generated values of $K_S^0$ momentum is shown in Figure 3.35. The division of the histogram in Fig. 3.34 by the one in Fig. 3.35 yields the fractions of reconstructed candidates for each momentum bin or efficiency distribution. It is illustrated in Figure 3.36.

Figure 3.37 contains the spectra obtained by bin-by-bin double Gaussian fit integral counting for on peak and off peak data samples. Figure 3.38 shows the result of the subtraction of off peak spectrum from on peak spectrum. It is the spectrum of $K_S^0$ coming from $\Upsilon(4S)$ decays (points with crosses) and it is overlayed with the generic $b\overline{b}$ Monte Carlo reconstructed $K_S^0$ spectrum (hollow crosses).

To get the differential multiplicities the histogram in Figure 3.38 should be divided by the histogram in Figure 3.36 or efficiency of the reconstruction. The division by the efficiency makes the result independent of the detector characteristics and it is sometimes called "unfolding" of the spectrum. Thus the spectrum of the $K_S^0$s coming from $\Upsilon(4S)$ decays is calculated and it is shown in Figure 3.39.

## 3.8 Branching ratio calculation

To calculate the overall branching fraction of the inclusive B meson decays to $K_S^0$ the following formula was used:

$$Br(B\overline{B} \to K^0_S X) =$$

$$= \frac{\frac{1}{eff_{K^0_S} \pm \delta(eff)} \times ((N^{K^0_S}_{on\,peak} \pm \delta N) - (N^{K^0_S}_{off\,peak} \pm \delta N) \cdot (L \pm \delta L) \cdot \frac{S_0}{S})}{2 \cdot (N_{BB} \pm \delta N_{stat} \pm \delta N_{syst})} \tag{3.8.1}$$

In this formula, $N^{K^0_S}_{on\,peak}$ and $N^{K^0_S}_{off\,peak}$ are the numbers of $K^0_S$ candidates that pass the analysis selection on peak and off peak, respectively.

$N_{BB}$ is the number of $B\overline{B}$ pairs counted by the Lumi script [30] (discussed in chapter 3.2).

$eff_{K^0_S}$ is the the efficiency of $K^0_S$ reconstruction estimated from Monte Carlo data.

$L \cdot \frac{S_0}{S}$ is the coefficient to account for the fraction of luminosities between on peak and off peak data samples and the difference of the continuum production cross-sections on $\Upsilon(4S)$ peak energy and off peak energy.[7]

Each term has its own errors that are discussed in the next section.

Here it is worth noting that the formula (3.8.1) provides the fraction of $K^0_S$ decaying through $\pi^+\pi^-$ per $B$ meson. For example if on average there are two $K^0_S \to \pi^+\pi^-$ decays per each $B$ meson produced the formula (3.8.1) will give $Br(B\overline{B} \to K^0_S X) = 2$. This illustrates the statement made in the chapter 3.1 that the quantity in formula (3.8.1) should be called multiplicity. However for heavy particles multiplicity is in most cases less than one. That is why the word "Branching Fraction" is conventionally used interchangeably with the word "multiplicity" in this case.

[7] Off peak is about 40 MeV lower.

## 3.9 Systematic and Statistical Errors

In this section the statistical and systematic errors are discussed. The errors in the formula (3.8.1) can be classified in two groups - statistical errors and systematic errors.

The following errors are statistical:

1. $\delta N^{K^0_S}_{on\,peak}$ - the statistical error on the number of $K^0_S$ the analysis selects on peak. From the Table 3.4 this error is 0.93% for sideband subtraction method of counting. This error is just a statistical Poisson error on the total number of candidates in the peak region and in the sideband regions. For single Gaussian fit counting method this error represents and error on the fit itself and it is 1.01%.

2. $\delta N^{K^0_S}_{off\,peak}$ - the statistical error on the number of $K^0_S$ the analysis selects off peak. Again as we can infer from Table 3.4 this error is 1.18% and 1.34% for sideband subtraction and Gaussian fit counting methods correspondingly.

3. $\delta N_{BBstat}$ - the statistical error of the B-counting. This error is quoted in Table 3.1. It is calculated by the lumi script [30] and it is equal to 0.93%

The following errors are systematic:

1. $\delta(eff_{K^0_S})$ - error on efficiency estimation through the Monte Carlo. It consists of two independent parts: the error of the candidate counting

in the Monte Carlo sample, and the tracking efficiency error. The latter is estimated to be about $\sim 1\%$ for the particular data sample used in this analysis [32]. The candidate counting error is listed in the Table 3.3 and it is 0.7 % for the double Gaussian fit counting.

2. $\delta L$ - error on Luminosity fraction estimation. This error is estimated by the Lumi counting script and is about 1.5%. With the release of improved software analysis packages this error is expected to go down to $\sim 1\%$.

3. $\delta N_{BBsyst}$ - the systematic error of the B-counting. Also given by lumi script. Taken from Table 3.1, it is about 1.6%.

In addition to the listed, several other systematic errors have been considered, for example the systematic errors on $K_S^0$ counting. However, they have been found to be insignificant compared with Gaussian statistical errors and thus have been disregarded.

## 3.10 Discussion of the results

Table 3.4 contains the results of $K_S^0$ counting by the analysis from the selected data samples, i.e., the parameters ($N^{K_S^0}_{on\,peak} \pm \delta N^{K_S^0}_{on\,peak}$) and ($N^{K_S^0}_{off\,peak} \pm \delta N^{K_S^0}_{off\,peak}$) from branching fraction formula (3.8.1).

Thus, all the necessary information is obtained to calculate the value of $Br(B\overline{B} \rightarrow K_S^0 X)$ and it is listed in table 3.5 for three methods of $K_S^0$ counting: single Gaussian, double Gaussian and sideband subtraction.

| Data Sample | Number of $K_S^0$ |
|---|---|
| On Peak Data | 98697±994 (single Gaussian Fit) |
| | 108399±329 (double Gaussian Fit) |
| | 108567 ±1013 (Sideband Subtraction) |
| Off Peak Data | 55618±746 (single Gaussian Fit) |
| | 61122±247 (double Gaussian Fit) |
| | 61402±727 (Sideband Subtraction) |

Table 3.4: *The output of the analysis run over the selected data samples.*

| Method of counting used | The Integrated multiplicity with stat. and syst. errors |
|---|---|
| Double Gaussian Fit | $0.216 \pm 0.003 \pm 0.015$ |
| Single Gaussian Fit | $0.222 \pm 0.009 \pm 0.025$ |
| Sideband Subtraction | $0.218 \pm 0.008 \pm 0.022$ |

Table 3.5: *Branching fraction* $Br(B\overline{B} \rightarrow K_S^0 X)$ *calculated using formula (3.8.1). Three results for three methods of* $K_S^0$ *counting are presented.*

In chapter 3.7 the dependence of the $Br(B\overline{B} \rightarrow K_S^0 X)$ on $K_S^0$ momentum was studied. $K_S^0$ multiplicities are calculated for different candidate momenta and that is why they are called differential multiplicity as opposed to integrated multiplicity calculated in table 3.5.

From the Table 3.5:

$$Br(B\overline{B} \rightarrow K_S^0 X) = 0.216 \pm 0.003 \pm 0.021$$

This translates to the overall branching fraction for $K^0$ mesons to be

$$Br(B\overline{B} \to K^0 X) = 0.630 \pm 0.009 \pm 0.043$$

This result is in good agreement with previous ARGUS' measurement $Br(B\overline{B} \to K^0 X) = 0.642 \pm 0.010 \pm 0.042$ [23].

We combine our value of the $Br(B\overline{B} \to K^0 X)$ with ARGUS' in the equation (1.5.6) from chapter 1.5 to obtain:

$$Br(B \to K^0/\overline{K}^0 X) - Br(B \to X_c \to K^0/\overline{K}^0 X) = 0.042 \pm 0.063$$

Here contributions to the branching ratio for $s$ production through charm are assumed to be $Br(B\overline{B} \to Charm \to K^0 X) = 0.594 \pm 0.056$ [26]. The experimental uncertainties on the value of Br$(B\overline{B} \to Charm \to K^0 X)$ come from $B \to D, D_s, \Lambda_c$ measurements that are expected to be significantly improved in the near future by *BABAR* and Belle. Another significant error is factored in through the $ss$-popping ($ss$ pair hadronic production) Monte Carlo calculation [33], [34] and it should also be improved as the understanding of the underlying physics improves with new results from b-factories. Overall, it is highly possible that the excess of neutral kaons in B decays will soon be measured with a separation of $\sigma - 2\sigma$. Combined with already observed excess of charged kaons of the magnitude of $3\sigma - 3.5\sigma$ this measurement would validate the hypothesis of "new physics" chromomagnetic dipole effects.

Another promising search strategy for enhanced $b \to sg$ is the measurement of high momentum kaon spectra. Figure 1.5 (b) in chapter 1.5

shows that the predicted new physics enhancement for kaons with momenta $p_K \geq 1.8\,\mathrm{GeV/c}$ is of order of the Standard Model background. To measure the tip of the kaon spectrum one needs much larger data sample and efficient selection method that should skim through the events to record only high momentum $K^0_S$ candidates. The efficiency of the reconstruction should be estimated from the Monte Carlo events specifically tuned to the task of finding high momentum $K^0_S$. Thus, the analysis of the tip of the spectrum is different in many ways from the one presented in this thesis but it is certainly very interesting to measure. This measurement seems very plausible with the current amounts of data collected at *BABAR* and hopefully will be performed in the near future.

# Chapter 4

# Conclusions

Studies of inclusive $B$ meson decays to $K_S^0$ are presented in this thesis. $B$ mesons are produced by the BABAR experiment through the $\Upsilon(4S)$ resonance at the asymmetric $e^+e^-$ collider - PEPII.

One of the significant physics results presented here is the $K_S^0$ spectrum and/or differential multiplicities in $K_S^0$ momentum bins. The results compare well with previous measurements and are illustrated in Figure 3.39.

The other and the most important result in this thesis is the inclusive $K_S^0$ branching fraction

$$Br(B\overline{B} \to K_S^0 X) = 0.216 \pm 0.003 \pm 0.021,$$

and the overall branching fraction for $K^0$ mesons

$$Br(B\overline{B} \to K^0 X) = 0.630 \pm 0.009 \pm 0.043.$$

These results do not show the clear excess of neutral kaons if the expected contribution via charm is subtracted and more work is needed to improve the

understanding of the theoretical topic of $b \to sg$. For example, better precision of branching fractions of bottom to charm. Three dominant systematic errors for $\mathrm{Br}(B\overline{B} \to K^0_S X)$ are errors on luminosity estimation, $B\overline{B}$ counting and Monte Carlo efficiency estimation (together with the reconstruction efficiency). There has been a progress made recently in the luminosity estimation as well as reconstruction efficiency resulting in the possibility of improving the overall error on $\mathrm{Br}(B\overline{B} \to K^0 X)$ by $\sim 20\%$. Currently the author is actively pursuing the work on improving the understanding of systematics of the $B\overline{B} \to K^0_S X$ within the BABAR inclusive hadronic spectra working group. To give a comprehensive answer to the puzzle of enhanced $b \to sg$ two additional approaches should be examined: the study of the high momentum tip of the $K^0_S$ spectrum and the study of charged kaons. This work is planned or being carried out at *BABAR* but it is wider than the scope of this thesis.

# Bibliography


[1] A. L. Kagan, Hints for Enhanced $b \to sg$ from Charm and Kaon Counting, hep-ph/9701300 (1997).

[2] J. H. Christenson et al., Phys. Rev. Lett. 13, 138 (1964).

[3] M. Kobayashi and T. Maskawa, *CP Violation In The Renormalizable Theory Of Weak Interaction*, Prog. Theor. Phys. **49**, 652 (1973).

[4] I. I. Y. Bigi et al., *CP violation: Advanced Series on Directions in High Energy Physics*, **Vol 3** p.175, World Scientific, Singapore (1989).

[5] R. G. Sachs, *The Physics of Time Reversal*, University of Chicago Press, Chicago (1987).

[6] A. D. Sakharov, Zh.E.T.F. Letters, **5** p.32, (1967).

[7] K. Kainulainen, T. Prokopec, M. G. Schmidt and S. Weinstock, *First principle derivation of semiclassical force for electroweak baryogenesis*, JHEP 06(2001)031.

# Bibliography


[1] A. L. Kagan, Hints for Enhanced $b \to sg$ from Charm and Kaon Counting, hep-ph/9701300 (1997).

[2] J. H. Christenson et al., Phys. Rev. Lett. 13, 138 (1964).

[3] M. Kobayashi and T. Maskawa, *CP Violation In The Renormalizable Theory Of Weak Interaction*, Prog. Theor. Phys. **49**, 652 (1973).

[4] I. I. Y. Bigi et al., *CP violation: Advanced Series on Directions in High Energy Physics*, **Vol 3** p.175, World Scientific, Singapore (1989).

[5] R. G. Sachs, *The Physics of Time Reversal*, University of Chicago Press, Chicago (1987).

[6] A. D. Sakharov, Zh.E.T.F. Letters, **5** p.32, (1967).

[7] K. Kainulainen, T. Prokopec, M. G. Schmidt and S. Weinstock, *First principle derivation of semiclassical force for electroweak baryogenesis*, JHEP 06(2001)031.

[8] J. M. Cline, M. Joyce, K. Kainulainen, *Supersymmetric Electroweak Baryogenesis*, hep-ph/0006119.

[9] M. Joyce and T. Prokopec *Baryogenesis from 'electrogenesis' in a scalar field dominated epoch*, JHEP 10(2000)030.

[10] J. McDonald *Q-ball Evolution, B-ball Baryogenesis and the $f_B$ Problem*, hep-ph/0012369.

[11] A. Einstein, B. Podolsky, N. Rosen, Physical Review 41, 777 (1935).

[12] The *BABAR* Collaboration, Observation of CP violation in the neutral B meson system, SLAC-PUB-8904, hep-ex/0107013, (July 5, 2001).

[13] The Belle Collaboration, Observation of Large CP Violation in the Neutral B Meson System, Belle preprint 2001-10, hep-ex/0107061, (July 23, 2001).

[14] B. Kayser, CP Violation in the K and B Systems, p.6, NSF-PT-96-2, November 1996.

[15] B. Kayser, CP Violation and Quantum Mechanics in the B System, FERMILAB-CONF-95-287-T.

[16] I. Dunietz, Phys. Rev. D **52**,3048 (1995).

[17] P. Oddone, B-Factories: A Personal Overview, *Prepared for Workshop on B-Factories and Related Physics Issues, Blois, France, 26 Jun - 1 Jul 1989.*

[18] P. Oddone, Detector Considerations, *IN *LOS ANGELES 1987, PROCEEDINGS, LINEAR COLLIDER B ANTI-B FACTORY CONCEPTUAL DESIGN* 423-446.* .

[19] HERA-B, *Design Report*, January 1995, DESY-PRC 95/01.

[20] The *BABAR* Collaboration, *Technical Design Report*, March 1995, accessible on www http://www.slac.stanford.edu/BFROOT/doc/TDR.

[21] The *BABAR* Collaboration, *The BABAR physics book*, (October 1998).

[22] Belle collaboration, *Technical Design Report*, KEK Report 95-1, (March 1995).

[23] H. Albrecht et al., ARGUS Coll., Z. Phys. C 62, 371 (1994).

[24] M. Ciuchini et al., Phys. Lett. 334B, 137 (1994).

[25] A. L. Kagan, Phys. Rev. D51,6196 (1995).

[26] A. L. Kagan, The Phenomenology of Enhanced $b \to sg$, hep-ph/9806266 (1998).

[27] G. Altarelli and S. Petrarca, Phys. Lett. B 261B 303 (1991).

[28] M. S. Alam et al., CLEO Collaboration, Phys. Rev. Lett 58,1814 (1987).

[29] R. M. Barnett at al., Particle Data Group, Phys. Rev. D54, 1 (1996).

[30] C. Hearty, Hadronic Event Selection and B-Counting for Inclusive Charmonium Measurements, BABAR B.A.D. number 30, (2000).

[31] R. Faccini et al., Studies on $K_S^0 \to \pi^+\pi^-$ reconstruction, BABAR B.A.D. number 19, (2000).

[32] BABAR B.A.D. number 54, (2001). BABAR B.A.D. number 61, (2000). BABAR B.A.D. number 87, (2001), BABAR B.A.D. number 157, (2001).

[33] A. L. Kagan and J. Rathsman, [phep-ph/9701300].

[34] K. Hamacher and M Weierstall (DELPHI Collaboration), DELPHI 95-80.